A three-sodium-to-glycine stoichiometry shapes the structural relationships of $ATB^{0,+}$ with GlyT2 and GlyT1 in the SLC6 family

Bastien Le Guellec[1†], **France Rousseau**[1†], **Marion Bied**[1], **Stéphane Supplisson**[1*]

***For correspondence:** stephane.supplisson@bio.ens.psl.eu (SS)

[†]These authors contributed equally to this work

[1]Institut de Biologie de l'ENS (IBENS), Inserm, CNRS, École normale supérieure, PSL Research University, Paris, France

Abstract $ATB^{0,+}$ (*SLC6A14*) absorbs all neutral and cationic amino acids in the distal colon and lung epithelia, and is part of the amino acid transporter branch I of the SLC6 family with GlyT1 (*SLC6A9*) and GlyT2 (*SLC6A5*), two glycine-specific transporters coupled to 2:1 and 3:1 Na^+:Cl^-, respectively. However, $ATB^{0,+}$ stoichiometry that specifies its driving force and electrogenicity remains unsettled. Using the reversal potential slope method, here we demonstrate that $ATB^{0,+}$-mediated glycine transport is coupled to 3 Na^+ and 1 Cl^- and has a charge coupling of 2.1 *e*/glycine. $ATB^{0,+}$ behaves as a unidirectional transporter with limited efflux and exchange capabilities. Analysis and computational modeling of the pre-steady-state charge movement reveal higher sodium affinity of the apo-$ATB^{0,+}$, and a locking trap preventing Na^+ loss at depolarized potentials. A 3 Na^+/ 1 Cl^- stoichiometry substantiates $ATB^{0,+}$ concentrative-uptake and trophic role in cancers and rationalizes its structural proximity with GlyT2 despite their divergent substrate specificity.

Introduction

Several Na^+-coupled amino acid transporters mediate the active uptake of glycine, which, despite its chemical simplicity - a nonessential amino-acid, without a side-chain or stereoisomer, and a membrane-impermeable zwitterion at physiological pH (***Chakrabarti, 1994***) - is nevertheless (1) a complex signaling molecule in the CNS as a fast inhibitory neurotransmitter and an agonist of the NR1 and NR3 subunits of the NMDA receptors (***Legendre, 2001***; ***Zeilhofer et al., 2012***; ***Johnson and Ascher, 1987***; ***Chatterton et al., 2002***; ***Grand et al., 2018***), (2) a key organic osmolyte for the regulation of cell volume in early embryos (***Dawson et al., 1998***), and (3) an essential metabolite for cell growth (***Wang et al., 2013***). Profiling studies have identified an increase in glycine one-carbon metabolism as an early warning signal of the rapid cell proliferation in cancers (***Jain et al., 2012***; ***Locasale, 2013***; ***Amelio et al., 2014***).

Three of these glycine transporters (GlyT1, GlyT2, and $ATB^{0,+}$) and the proline transporter (PROT) are clustered in the amino-acid transporters branch (I) of the Solute Carrier 6 (SLC6) family, also named Neurotransmitter:Sodium Symporters (NSS) (***Bröer and Gether, 2012***). GlyT1 and GlyT2 correspond to the classic, high-affinity and glycine-specific "system Gly", while $ATB^{0,+}$ lacks substrate specificity (***Christensen, 1990***) and transports a broad variety of α and β amino acids, D- and L-amino acids, amino acid derivatives, and pro-drugs (***Sloan and Mager, 1999***; ***Winkle et al., 1985***; ***Hatanaka et al., 2001***; ***Nakanishi et al., 2001***; ***Hatanaka et al., 2002***, ***2004***; ***Anderson et al., 2008***).

This broad specificity suggests that $ATB^{0,+}$ has a distinctive substrate site from the one of GlyT1 and GlyT2, but nevertheless, we refer to $ATB^{0,+}$ as a glycine transporter for simplicity.

GlyT1 and GlyT2 recapture and recycle glycine released at fast inhibitory synapses in the spinal cord, brainstem and cerebellum (***Legendre, 2001***; ***Eulenburg et al., 2005***; ***Zeilhofer et al., 2012***; ***Ankri et al., 2015***). GlyT2 is a specific marker of glycinergic neurons and operates like a unidirectional glycine pump as its 3 Na^+/1 Cl^- stoichiometry provides an excessive driving force for influx (***Roux and Supplisson, 2000***; ***Supplisson and Roux, 2002***). GlyT2 inactivation disrupts the cytosolic accumulation and vesicular release of glycine (***Gomeza et al., 2003***; ***Rousseau et al., 2008***; ***Apostolides and Trussell, 2013***), and $GlyT2^{-/-}$ knockout mice develop a severe hypoglycinergic syndrome (***Gomeza et al., 2003***) while mutations of human *SLC6A9* cause Hyperekplexia (OMIM:#614618), a rare neurological disorder with exaggerated startle reflexes (***Rees et al., 2006***; ***Carta et al., 2012***). In contrast, GlyT1 is as a bidirectional, 2 Na^+/1 Cl^--coupled transporter that is expressed primarily on astrocytes and behaves as a buffer, sink, or source of extracellular glycine (***Zafra et al., 1995***; ***Supplisson and Bergman, 1997***; ***Huang and Bordey, 2004***; ***Aubrey et al., 2005***, ***2007***; ***Sipilä et al., 2014***; ***Shibasaki et al., 2017***). However, GlyT1 concentrative uptake is sufficient to specify the glycinergic phenotype of retinal amacrine cell (***Eulenburg et al., 2018***), and critical for the cell volume regulation of early mouse embryos (***Steeves et al., 2003***; ***Steeves and Baltz, 2005***). On the extracellular side, GlyT1 tunes the basal concentration and spillover of glycine (***Sipilä et al., 2014***; ***Ahmadi et al., 2003***) that gate NMDARs activation depending on their subunits composition, synaptic location, brain structure, and developmental stage (***Supplisson and Bergman, 1997***; ***Supplisson and Roux, 2002***; ***Tsai et al., 2004***; ***Martina et al., 2005***; ***Papouin et al., 2012***; ***Bail et al., 2015***; ***Ferreira et al., 2017***; ***Otsu et al., 2019***). GlyT1-deficit leads to an hyperglycinergic phenotype with hypotonia and motor disorders in $GlyT1^{-/-}$-knockout mice and *Shocked* Zebrasfish-mutant (***Gomeza et al., 2003***; ***Tsai et al., 2004***; ***Cui et al., 2005***; ***Mongeon et al., 2008***; ***Hirata et al., 2010***; ***Eulenburg et al., 2010***). Mutations of human *SLC6A5* caused glycine encephalopathy with normal serum glycine (OMIM:#617301), a severe metabolic disease that produces hypotonia and respiratory failures in neonatal (***Kurolap et al., 2016***; ***Hauf et al., 2020***).

In comparison, the energetic and biophysical properties of $ATB^{0,+}$ remain undercharacterized. $ATB^{0,+}$ mediates electrogenic and concentrative uptakes of all neutral and cationic amino acids with Hill coefficients suggesting a 2 Na^+ and 1 Cl^- stoichiometry (***Sloan and Mager, 1999***; ***Hatanaka et al., 2001***; ***Nakanishi et al., 2001***; ***Karunakaran et al., 2008***). $ATB^{0,+}$ is expressed in the lung and distal colon epithelia, and in the mammary and pituitary glands (***Villalobos et al., 1997***; ***Sloan and Mager, 1999***; ***Ugawa et al., 2001***; ***Sloan et al., 2003***; ***Chen et al., 2020***). Mice lacking $ATB^{0,+}$ are viable and with normal phenotype (***Babu et al., 2015***; ***Ahmadi et al., 2018***), but genome-wide association studies have identified SNPs in non coding regions of *SLC6A14* that are linked to obesity (***Suviolahti et al., 2003***; ***Corpeleijn et al., 2010***; ***Sivaprakasam et al., 2021***), male infertility (***Noveski et al., 2014***), and the phenotypic variation and severity of cystic fibrosis (***Sun et al., 2012***; ***Corvol et al., 2015***). In particular, the lack of $ATB^{0,+}$ impairs intestinal fluid secretion in the context of cystic fibrosis and is responsible of Meconium Ileus at birth (***Ahmadi et al., 2018***; ***Ruffin et al., 2020***). Ganapthy's group has demonstrated the implication of $ATB^{0,+}$ in cancers, as one of the four amino-acid transporters with *SLC1A5*, *SLC7A5*, *SLC7A11* that are up-regulated in tumors for matching the increased demand in amino acids for cell growth, and more particularly for glutamine and glycine (***Bhutia et al., 2014***; ***Coothankandaswamy et al., 2016***; ***Sikder et al., 2017***; ***Sniegowski et al., 2021***).

Here, we investigated the stoichiometry and exchange mode of $ATB^{0,+}$ in order to better evaluate its driving force and transport properties under physiological and pathological conditions. An additional motive was to understand the raison d'être of the surprising structural hierarchy between these three glycine transporters of the SLC6 family. We used the reversal potential of $ATB^{0,+}$ in order to establish its stoichiometric coefficients by a thermodynamic method. Our results revise the apparent consensus for a 2 Na^+ stoichiometry, and the charge/glycine and charge movement in glycine-free media confirmed the higher Na^+ coupling. Finally, we show that 3 Na^+-coupling reduces both the efflux and exchange of glycine in $ATB^{0,+}$ and GlyT2-expressing oocytes, a property

that is not shared by other 3 Na^+-coupled transporters like the glutamate transporter EAAT2 who operates by a distinct elevator mechanism (***Kavanaugh et al., 1997***; ***Drew and Boudker, 2015***).

Results

Odd phylogenetic and functional relationships of $ATB^{0,+}$ with GlyT1 and GlyT2

The position of $ATB^{0,+}$ in the phylogenetic tree of SLC6 transporters (***Figure 1***A), closer to GlyT2 than this one is of GlyT1, seems at odds with their marked functional divergence in terms of specificity and affinity for glycine, as detailed below and in the next paragraph. Although the length of the common branch is short (0.14 for $ATB^{0,+}$/GlyT2 *vs.* 0.07 for GlyT1/PROT, ***Figure 1***A), the same split is nonetheless observed for all Vertebrates orthologs despite a greater divergence in $ATB^{0,+}$ sequences (***Figure 1***A-B). Indeed, the percentage of identities (ID) between orthologs is lower for $ATB^{0,+}$ (39 % ID) than for GlyT2 (69.7 % IDs) and GlyT1 (60.3 % ID) as shown in***Figure 1***B. A higher divergence is also detected in the more conserved transmembrane segments with 46.5 % *vs.* 77.3 %, and 70 % IDs, respectively ***Figure 1–Figure Supplement 1***A. Venn diagrams of private and shared residues confirm that mGlyT2 shares more IDs with $mATB^{0,+}$ (n = 95) than with mGlyT1 (n = 76, ***Figure 1***C, ***Figure 1–Figure Supplement 2***) and the GlyT2/$ATB^{0,+}$ pair shows a similar excess for each ortholog (+15.5±1.1 ID, n = 8, ***Figure 1–Figure Supplement 1***B). PROT was included in the analysis to count only for IDs specific of a glycine-transporter pair (GlyT2/$ATB^{0,+}$: 55.4±1.1 ID, GlyT2/GlyT1: 39.9±1.5 ID, $ATB^{0,+}$/GlyT1: 25.5±1.5 ID, n = 8, ***Figure 1–Figure Supplement 1***B).

The substrate site of $ATB^{0,+}$ is expected to differ substantially from the one of GlyT1 and GlyT2 as it can accommodate a large variety of amino acids size and side chains, with aliphatic, cationic, hydrophobic, or hydrophilic properties. Indeed, all the natural amino acids at the exception of glutamate and aspartate evoke an inward current in $ATB^{0,+}$-expressing oocytes, in contrast to the absolute glycine specificity of GlyT1 and GlyT2 (***Figure 1***D). Therefore, other factors than a common substrate site for glycine must explain the structural proximity of $ATB^{0,+}$ and GlyT2. Nevertheless, it is worth noticing that both transporters share the same intolerance for N-methyl-derivative while GlyT1 transports sarcosine (***Figure 1***D).

$ATB^{0,+}$ glycine-EC_{50} shows an anomalous voltage-dependency

Glycine evokes inward currents in $ATB^{0,+}$-expressing oocytes that do not reverse up to +50 mV (***Figure 2***A), and are strictly dependent on Na^+ and Cl^- (***Figure 2–Figure Supplement 1***). The current-voltage relationship is quasi-linear at saturating glycine concentration, indicating a weak voltage-dependency of its transport cycle similar to GlyT1 and GlyT2 (***Figure 2***B), with efold of 296, 313, and 254 mV, respectively.

In contrast, $ATB^{0,+}$ dose-response-curve for glycine shows a distinct and lower apparent affinity, with a more complex voltage-dependency than for GlyT1 and GlyT2 (***Figure 2***C-D) as previously reported in ***Roux and Supplisson*** (***2000***). In particular, $ATB^{0,+}$-EC_{50} shows a minimum at −20 mV (171±4 µM, n = 6), and then increases at both, depolarized and hyperpolarized potentials, whereas GlyT2- and GlyT1-EC_{50} are voltage-independent in the negative range (***Figure 2***D, ***Roux and Supplisson*** (***2000***)).

On average, a saturating glycine concentration evokes ~ 6-fold larger currents in $ATB^{0,+}$-expressing oocytes than for GlyT2 and GlyT1 (1450.0±98.8 pA (n = 65) *vs.* 250.0±29.7 pA (n = 48) , and 245.2±17.3 pA (n = 85) at V_H =−40 mV for 1–2 mM ($ATB^{0,+}$) and 200 µM (GlyT2, GlyT1), respectively, ***Figure 3***A). Therefore, we examined whether the membrane-expression, charge per glycine, and turnover-rate can account for $ATB^{0,+}$ larger electrogenicity.

$ATB^{0,+}$ and GlyT2 share similar charge movements

We used the charge-movement of $ATB^{0,+}$ as a proxy of their cell-surface expression in *Xenopus* oocytes. The ***Figure 3***B shows representative traces of the presteady-state currents (PSSCs) of GlyT1, GlyT2 and $ATB^{0,+}$ rthat are ecorded in glycine-free media and isolated using their specific

inhibitors (ORG24598, ORG25543 and α-Methyl-D,L-tryptophan (αMT), respectively) to subtract the oocyte endogenous-currents. It could be noticed that $ATB^{0,+}$ and GlyT2 share asymmetric PSSCs, with large outward-currents and biphasic time-courses, whereas GlyT1-PSCCs are weakly voltage-dependent (***Figure 3***B).

The charge movement plotted as function of voltage (*Q-V*) confirms the likeness of $ATB^{0,+}$ and GlyT2, with the same slope and clear evidence of saturation (***Figure 3***C). Fits of *Q-V*s with a Boltzmann equation (2) show similar apparent charge (z_{max}) for $ATB^{0,+}$ (1.26±0.02 *e*, n = 38) and GlyT2 (1.25±0.01 *e*, n = 53) that are almost one charge higher than for GlyT1 (0.37±0.02 *e*, n = 14, ***Figure 3***D). The potential of half distribution ($V_{1/2}$) is positive for $ATB^{0,+}$ (+16.2±0.9 mV, n = 38) and right-shifted relative to GlyT2 and GlyT1 (−35.0±0.8 mV (n = 5) and −17.3±3.3 mV (n = 14), respectively, ***Figure 3***E). Finally, the average $ATB^{0,+}$-Q_{max} is 2.4-fold larger than for GlyT2 (44.0±2.8 nC (n = 38) *vs.* 18.6±1.3 nC (n = 53), respectively ***Figure 3***F), thus confirming $ATB^{0,+}$ higher cell-surface expression.

Overexpression of membrane transporters can expand the cell-surface of injected oocytes (***Hirsch et al., 1996***), we compared the linear membrane capacitance (Cm) of non-injected oocytes (207±3 nF, n = 33) with oocytes expressing GlyT1 (227±7 nF, n = 11), GlyT2 (243.0±5.2 nF, n = 10), and $ATB^{0,+}$ (301.0±6.3 nF, n = 50, p<0.001) ***Figure 3–Figure Supplement 1***C. As the membrane capacitance is known to be proportional to the surface area (Cm = 1 μF/cm^2), the ∼45 % increase in Cm suggests a similar expansion of surface area in oocytes expressing $ATB^{0,+}$.

A thermodynamic determination of $ATB^{0,+}$ stoichiometric coefficients

To establish the stoichiometric coefficients of each cosubstrate, we adapted to $ATB^{0,+}$ the reversal potential slope method (e.g., ***Appendix 1***) that successfully solved the stoichiometry of EAAT3, GlyT1, and GlyT2 (***Zerangue and Kavanaugh, 1996***; ***Roux and Supplisson, 2000***). For this, it was first necessary to alter the intracellular composition of oocytes by micoinjection and find a set of intracellular concentrations able to reduce the excessive driving force of $ATB^{0,+}$ and shift its reversal potential below +50 mV.

Initial attempts with a small nanoliter-volume injection of glycine (1 M) sufficient to evoke an outward currents in GlyT1-expressing oocytes, failed to reverse $ATB^{0,+}$ nor GlyT2 ***Figure 4***A,B. Further addition of NaCl in the pipette solution that strongly reduced $ATB^{0,+}$ driving-force as indicated by the lower amplitude of the transport current evoked by a second glycine application, triggers small outward currents at −20 mV in GlyT2- and $ATB^{0,+}$-expressing oocytes (***Figure 4***A,B). Eventually, we selected injection parameters that evoked robust and steady outward currents in $ATB^{0,+}$-expressing oocytes (***Figure 4***C). These transporter-mediated currents are isolated by subtraction with αMT ***Figure 4***CD, and are bidirectional, with a stable and measurable reversal potential (***Figure 4***D, blue triangles)) that is sensitive to extracellular manipulation of each cosubstrate concentration.

Using this experimental paradigm, we impaled two electrode voltage-clamp oocytes expressing $ATB^{0,+}$ with a third micropipette and injected 13–23 nL of solution containing 0.5 M NaCl and glycine. As a steady outward current develops following injection, we constructed three I-Vs for each oocyte with either a change in glycine (2, 0.2, and 0.02 mM, ***Figure 5***A), Na^+ (100, 30, and 10 mM, ***Figure 5***B), or Cl^- (100, 30, and 10 mM, ***Figure 5***C) and the current reversal potentials were plotted in linear-log plots for each cosubstrate (***Figure 5***D). Regression analysis show similar slopes for glycine (28.6±1.0 mV/decade, n = 8) and Cl^- (31.5±2.7 mV/decade, n = 6), but much steeper for Na^+ (84.7±4.5 mV/decade, n = 11 ***Figure 5***D). The average stoichiometric coefficients determined by the slope ratios (n_{Gly}= 1.0±0.1 , n_{Cl}= 1.1±0.1 , and n_{Na}= 2.9±0.2 , ***Figure 5***E) support a 3 Na^+, 1 Cl^-, 1 glycine stoichiometry for $ATB^{0,+}$.

In agreement, we measured a charge coupling (z_T) of 2.08 *e*/glycine from the slope of the linear relationship between the time-integral of the transport current and ^{14}C glycine uptake, thus confirming the tight electrogenic coupling of $ATB^{0,+}$ transport-cycle (***Figure 5–Figure Supplement 1***A). Finally, an apparent turnover rate (λ = 18 s^{-1}) was estimated from the linear relationship between I_{max} and Q_{max} (29.7 s^{-1}), after correction for the ratio of glycine-coupled/glycine-uncoupled charges (see

Figure 5–Figure Supplement 1B). Together, the charge coupling and turnover rate of $ATB^{0,+}$ well predict the current amplitude for an average expression in oocyte ($Q_{\max}$ = 44 nC) as $I_{\max} = Q_{\max}\frac{z_T}{z_{\max}}\lambda =$ 1307 nA), within the range reported in ***Figure 3***A.

An external gate controls the access and locking of Na^+ sites in the apo-$ATB^{0,+}$

Evidence from the shift in *Q-V*s (***Figure 3***E) as well as from the abnormal rectification of the glycine-EC_{50} at negative potentials (***Figure 2***D) suggests an higher sodium affinity of the apo outward-facing conformation of $ATB^{0,+}$, and more complex allosteric interactions with Na^+ than for GlyT2. Therefore, we examined in more details the Na^+- and voltage-dependence of $ATB^{0,+}$ and GlyT2 charge-movement.

The ***Figure 6***A shows a marked and unexpected reduction in the envelope of $ATB^{0,+}$-PSSCs for a tenfold reduction in sodium concentration. The upper range of the voltage steps was extended to +110 mV in order to catch evidence of saturation, such as the current-crossing as the charge movement approached saturation but not the current peak-amplitude (***Figure 6***A). Traces in ***Figure 6***A show that a marked current-crossing at 100 mM and 50 mM Na^+ that is strongly reduced at 20 mM and absent at 10 mM.

According to a minimal two-state Hill model for multiple Na^+ proposed for GAT1 (***Mager et al.*** (***1996***, 1998)), and corresponding to the scheme #1 in ***Figure 6–Figure Supplement 1***A), a ten-fold reduction in [Na^+] is predicted to left-shift the *Q-V* without altering its slope nor $Q_{\max}$ (***Mager et al., 1996***). Although individual fits with a Boltzmann equation support this prediction for GlyT2 (***Figure 6–Figure Supplement 2***A-B), this is not the case for $ATB^{0,+}$ as shown by the decreasing peaks of the *Q-V* first derivative (***Figure 6–Figure Supplement 2***C-D). As expected, the scheme #1 generates a poor global fit of $ATB^{0,+}$ *Q-V*s as function of Na^+, while being acceptable for GlyT2 ***Figure 6–Figure Supplement 3***A).

Then we tested a sequential, linear model that preserves Hill formalism for simplicity, with a single and voltage-dependent binding step for multiple Na^+ with a charge $z\beta$, but includes a gating step controlling the access to or priming of Na^+-sites for binding (schemes #2 and #3, ***Figure 6–Figure Supplement 1***A). Gate opening and closure are voltage-dependent with $z\alpha$ the charge of the gating step ($U \longleftrightarrow U^c$) of Na^+ unbound transporters and $z\gamma$ the charge displacement that lock Na^+ ($B \longleftrightarrow B^c$) (***Figure 6–Figure Supplement 1***A) .

Because these two-path exits from the Na^+-bound state (B) at positive potentials could carries asymmetric charges ($z\gamma > z\alpha + z\beta$), scheme #3 was able to solve the apparent Na^+-dependency of $z_{\max}$ (***Figure 6***D) as indicated by the overwhelming difference in Akaike criterion information (ΔAICc) tabulated in ***Figure 6–Figure Supplement 1***B. Furthermore, the scheme #3 describes also the constant $z_{\max}$ of GlyT2 *Q-V* (***Figure 6***D), as $z\gamma \leq z\alpha + z\beta$. Na^+ locking in the apo outward facing conformation of $ATB^{0,+}$ is further facilitated by an higher affinity for Na^+, with a 3.5 fold difference in Kd (23 and 80 mM, for $ATB^{0,+}$ and GlyT2, respectively), whereas conversely, GlyT2 lower affinity facilitates gate closure primarily from the Na^+-unbound state U (***Figure 6–Figure Supplement 1***C,***Figure 6–Figure Supplement 4***). As expected for a linear model, extrapolations at extreme voltage (+2 V) confirm a convergence to the same $Q_{\max}$ value ***Figure 6–Figure Supplement 5***.

Globally, the fit parameters for $ATB^{0,+}$ and GlyT2 in the scheme #3 show a remarkable coherency (***Figure 6***B,C), with little difference in the Hill coefficients (2.3 and 2.4, for $ATB^{0,+}$ and GlyT2 respectively). Because it is a four-state model, the median voltage ($V_{med.}$) was estimated as function of [Na^+] (***Figure 6***D) as shown in ***Figure 6–Figure Supplement 6***) that is positive for [Na^+]> 40 mM for $ATB^{0,+}$ but always negative for GlyT2, up to 200 mM (***Figure 6***E), indicating that Na^+ binding in the absence of voltage is energetically favorable for $ATB^{0,+}$ while not for GlyT2 ***Figure 6***F.

Finally, we challenged the model #3 to reproduce the highly asymmetric and biphasic time courses of $ATB^{0,+}$ transient current using the fitted equilibrium constants and charges of ***Figure 6***B (see material and method). ***Figure 6***F shows simulations that effectively recapitulate the Na^+ dynamics of $ATB^{0,+}$ PSSCs, supporting further the gating and locking mechanisms of scheme #3.

3-Na^+ coupling limits efflux and exchange of glycine transporters

The driving force of a 3 Na^+-coupled transporter can support large flux asymmetry that favor a net influx while limiting a net efflux, although unidirectional efflux by homo- or heteroexchange is still possible as shown for glutamate transporters (***Kavanaugh et al., 1997***). Limiting heteroexchange would be beneficial for $ATB^{0,+}$ function considering its broad substrate specificity, by limiting futile cycles and leak of intracellular metabolites. Therefore, we compared the rate of glycine efflux and exchange in voltage-clamp oocytes pre-loaded with ^{14}C-glycine and hold at V_H = −60 mV in order to minimize the basal efflux rate. The rate of efflux of ^{14}C-glycine for each transporter was monitored in the outflow solution under basal condition and during glycine application (***Figure 7***A).f As expected from their difference in driving force, the basal glycine efflux was lower for $ATB^{0,+}$ and GlyT2 compared to GlyT1 (***Figure 7***,A,B). Application of glycine stimulated exchange of GlyT1-expressing oocytes as shown by the 8-fold increase in efflux rate (***Figure 7***A,B), while only slightly in GlyT2 and $ATB^{0,+}$-expressing oocytes (***Figure 7***A,B).

Discussion

Here, we establish a new 3 Na^+, 1 Cl^-, 1 amino acid stoichiometry for $ATB^{0,+}$ that supports its unidirectional and concentrative uptake properties, and provides a rationale for its structural proximity with GlyT2 in the SLC6 family.

A thermodynamic revision of $ATB^{0,+}$ stoichiometry

The charge-coupling of +2.08 *e*/glycine measured in $ATB^{0,+}$-expressing oocytes forced us to question the large consensus about its 2 Na^+, 1 Cl^- stoichiometry, as this charge is larger than predicted from this stoichiometry and required either (1) a third Na^+-coupling like GlyT2 (***Roux and Supplisson, 2000***), (2) a Cl^--exchange as proposed for GAT1 (***Loo et al., 2000***), or (3) a substrate-gated uncoupled-conductance as for the anion conductance of the glutamate transporters (***Wadiche et al., 1995b***; ***Cater et al., 2016***).

We used the reversal potential slope-ratio method that is based on the zero-flux equation (***Appendix 1***) and has successfully solved the stoichiometric coefficients of EAAT2-3, GlyT1-2 and GAT1 (***Zerangue and Kavanaugh, 1996***; ***Levy et al., 1998***; ***Roux and Supplisson, 2000***; ***Lu and Hilgemann, 1999***; ***Willford et al., 2015***). As previously reported for GlyT2, it was first necessary to reduce the excessive inwardly-directed driving force of $ATB^{0,+}$ at saturating glycine concentration (2 mM), as equation 6 predicts reversal potentials of 169 mV or 111 mV for a 2 or 3 Na^+/ 1Cl^--coupled transporter, respectively (assuming $[Gly]_i$ = 1 mM, $[Na^+]_i$ = 10 mM and $[Cl^-]_i$ = 35 mM). To find a set of intracellular concentrations that allow $ATB^{0,+}$ to operate bidirectionally, we routinely injected 22 nL solution of NaCl + glycine (0.5 M) that increases their concentration by ∼17.7 mM assuming an oocyte effective water-volume of 600 nL, that is sufficient to left-shift the current reversal potential to +32.8 mV or +33.1 mV for a 2 or 3 Na^+-coupling, respectively, which is in agreement with the average value of 32.5 mV in ***Figure 5***D.

The average reversal potential slope of 28.6 mV determined for a ten-fold reduction in $[Gly]_e$ is close to the theoretical slope of 29.6 mV for two charges at 25 °C (Equation 6), and confirms that they are both energetically coupled to the transport cycle. The slope values for Na^+ (84.6 mV/decade) and Cl^- (32 mV/decade) are also closed to the theoretical values for 3 Na^+/gly and 1 Cl^-/gly (88.4 and 28.6 mV/decade, respectively), thus establishing a 3 Na^+/1Cl^-/1 glycine stoichiometry for $ATB^{0,+}$.

Does $ATB^{0,+}$ need such a large driving force ?

The increase in driving force provided by a third Na^+ substantiates the "highly-concentrative" adjective often used to describe $ATB^{0,+}$-mediated uptake (***Barilli et al., 2020***; ***Gupta et al., 2005***; ***Hatanaka et al., 2001***; ***Karunakaran et al., 2008***, ***2011***). Nevertheless, a weaker driving force is predicted for $ATB^{0,+}$ than the up to a million fold glycine accumulation of GlyT2 (***Roux and Supplisson, 2000***; ***Supplisson and Roux, 2002***), because of the smaller amplitude of Na^+ and Cl^- electrochemical gradients in the colon and lung epithelia than in nerve terminals.

Located in the apical membrane of colonocytes in the absorptive epithelium (***D'Argenio et al., 2006***; ***Gupta et al., 2005***; ***Hatanaka et al., 2002***; ***Ugawa et al., 2001***), $ATB^{0,+}$ absorbs mixtures of amino acids issues from the bacterial proteolysis taking place in the outer mucus layer and lumen of the colon, and $ATB^{0,+}$ clearance of nutrients helps to maintaining an apparent sterility of the adherent inner mucus layer (***Atuma et al., 2001***; ***Johansson et al., 2008***; ***Jakobsson et al., 2015***; ***Li et al., 2015***; ***Chen et al., 2020***).

As over 90 % of NaCl and water that enter the cecum are reabsorbed in the proximal colon (***Phillips, 1969***; ***Thiagarajah and Verkman, 2018***; ***Sandle, 1998***), considerably lower [Na^+] (~15 mM) and [Cl^-] (<10 mM) have been measured at the surface of the rat distal colon (***Talbot and Lytle, 2010***; ***Chen et al., 2020***). If these concentrations correspond to those of the thin mucus layer, then a 3 Na^+-coupling is not an option but a requirement for $ATB^{0,+}$ in order to provide enough driving force for an uphill transport of amino acids since it would be minimal or even not possible otherwise (***Chen et al., 2020***).

In the lung, $ATB^{0,+}$ plays a similar scavenging role on the apical side of the airway epithelium (***Sloan and Mager, 1999***; ***Sloan et al., 2003***; ***Uchiyama et al., 2008***; ***Paola et al., 2017***), thus depleting essential nutrients and limiting bacteria growth in the thin and sterile airway surface layer (ASL) (***Mager and Sloan, 2003***; ***Paola et al., 2017***; ***Ruffin et al., 2020***). Short circuit currents evoked by amino acids and dependent on Na^+ have been recorded in cultured human bronchial epithelial cells and mouse trachea epithelium (***Galietta et al., 1998***; ***Sloan et al., 2003***; ***Ahmadi et al., 2019***), although the [Na^+] and [Cl^-] in the thin ASL are not precisely known as two opposing models predict either a low salt condition (~50 mM) or near isotonic concentrations (***Boucher, 1999***; ***Jayaraman et al., 2001***; ***Song et al., 2003***). In any event, the driving force generated by a 3 sodium-coupling should not be a limiting factor for $ATB^{0,+}$ scavenging function.

Upregulation of $ATB^{0,+}$ has been detected in twelve types of solid cancers (***Sikder et al., 2017***, ***2020***) suggesting that its overexpression is the main mechanism to increase the uptake rate of glutamine or glycine, because of the dynamic *cis* and *trans* competition when $ATB^{0,+}$ is exposed to mixture of amino acids. Furthermore $ATB^{0,+}$ overexpression in colon cancer leads to its misrouting to the basolateral side of the epithelium with unrestrained access to the serosal pool of amino acids (***Chen et al., 2020***).

Na^+ binding, locking and allosteric interactions

The charge movement of ion-coupled transporters is a substrate-free signature of their membrane expression and interactions with motor ions, as shown for SGLT1 (***Parent et al., 1992***; ***Loo et al., 1993***), GAT1 (***Mager et al., 1996***; ***Bossi et al., 2002***), EAAT2 (***Wadiche et al., 1995a***), NaPi-2 (***Forster et al., 1998***), GlyT1-2 (***Roux et al., 2001***; ***Cherubino et al., 2010***), GAT3 (***Sacher et al., 2002***), and SNAT2 (***Grewer et al., 2013***). The relaxation currents evoked by positive voltage steps correspond to electrogenic steps of the partial transport cycle that are associated with Na^+ unbinding, while conversely negative voltage steps drive Na^+ binding/occlusion in the outward-facing conformation of the apo-transporter (***Grewer et al., 2013***; ***Hilgemann and Lu, 1999***). In addition to ion displacement, the charge movement can involve the reorientation of charged residues that are confined within the membrane electric field (***Bezanilla, 2008***, ***2018***), as demonstrated by voltage-clamp fluorometry for SGLT1 and GAT1 (***Cowgill and Chanda, 2019***; ***Li et al., 2000***; ***Loo et al., 1998***; ***Meinild et al., 2009***).

Not surprisingly, the *Q-V*s of $ATB^{0,+}$ and GlyT2 confirms their common ionic coupling as they run parallels indicating similar charge displacement, which is almost one charge higher (+0.88 *e*) than for GlyT1, thus suggesting a net contribution of the third Na^+. Both transporters have Hill coefficient above 2, indicating a cooperativity of the three Na^+ sites. However, $ATB^{0,+}$ large difference in $V_{1/2}$ (+51 mV, ***Figure 3***D) and lower microscopic Kd (23 *vs.* 80 mM, ***Figure 6***B-C)) relative to GlyT2 indicate an higher affinity for Na^+. The fraction of Na^+-bound transporters at −40 mV is 94 % for $ATB^{0,+}$ while only 56 % for GlyT2 (closed circles in ***Figure 6–Figure Supplement 4***C). We show that both the slope and Q_{max} of $ATB^{0,+}$ are reduced at lower Na^+ concentrations, thus preventing a global

fit by the minimal two-state model proposed by ***Mager et al.*** (***1996***) for GAT1. Although such Na^+-dependency is unexpecte, it is nevertheless not unique as a similar reduction in slope and Q_{max} was reported for GAT3, yet uninterpreted with a kinetic model (***Sacher et al., 2002***). We show that addition of a gating and locking steps with asymmetric charges solve the apparent Na^+-dependency of $ATB^{0,+}$ *Q-V*. A dynamic equilibrium between the two Na^+-unbinding paths, with either its extracellular release or locking in the transporter as the external gate close, and a small imbalance between the valency of the two paths predict the reduction in z_{max} at low Na^+ concentrations. Conversely, the locking step plays little role for GlyT2 because of its lower affinity favored gate closure of Na^+-unbound transporters. It can be speculated that Na^+-locking in $ATB^{0,+}$, by preventing Na^+ release, stabilize Na^+-bound conformation at depolarized potentials.

Structural proximity of $ATB^{0,+}$ and GlyT2

A single serine residue (S481) in the unstructured central part of TM6, controls the substrate intolerance for N-methyl derivative of GlyT2 (***Vandenberg et al., 2007***). Indeed, sarcosine evokes a current in oocytes expressing GlyT2 mutants at this position (S481G or S481A) while introducing a serine abolishes sarcosine transport in the GlyT1 mutant G305S (***Vandenberg et al.*** (***2007***)). As expected from its intolerance to sarcosine (***Figure 1***D, ***Anderson et al.*** (***2008***)), $ATB^{0,+}$ has a serine (S320) at the equivalent position (***Figure 1–Figure Supplement 2***).

Although a detailed structure of a 3-Na^+-coupled NSS is not yet available, molecular dynamics simulations with plausible atomic models of GlyT2 based on dDAT crystal structure (***Penmatsa et al., 2013***), have identified several residues for the putative third Na^+ binding site (***Subramanian et al., 2016***; ***Benito-Muñoz et al., 2018***). In these models, the Na1 and Na2 sites correspond to those of dDAT (***Penmatsa et al., 2013***) and LeuTaa (***Yamashita et al., 2005***), close to the substrate site, allowing a direct coordination with the carboxyl of glycine, as found for leucine in the high-resolution structure of LeuTaa (***Yamashita et al., 2005***). In contrast, the proposed Na3 site is located more distantly from the substrate site and involves an electrostatic interaction with the glutamate E650 in TM10 (***Subramanian et al., 2016***; ***Benito-Muñoz et al., 2018***). It is worth noticing that $ATB^{0,+}$ shares the same glutamate residue at this position (E489, ***Figure 1–Figure Supplement 2***), whereas GlyT1 has a methionine (M470) that cannot engage in an electrostatic interaction with Na^+. The other putative residues proposed to coordinate the third Na^+ (M278, W265, A483 (***Subramanian et al., 2016***) or E250 (***Benito-Muñoz et al., 2018***)) are all identical for the three glycine transporters, suggesting that E489 is the primary specific candidate for the Na3 site of these two glycine transporters.

Methods and Materials

Molecular biology

Heterologous expression of SLC6 transporters in *Xenopus* oocytes

The cDNAs encoding the mouse $ATB^{0,+}$ (gift of V. Ganapathy, ***Hatanaka et al.*** (***2001***)), the rat GlyT2a (gift of B. Lopez Corcuera and C. Aragon, ***Liu et al.*** (***1993***)) and the rat GlyT1b (gift of K Smith, Synaptic, ***Smith et al.*** (***1992***)) were subcloned in a modified pRC/CMV vector as described previously in ***Supplisson and Bergman*** (***1997***). Capped cRNAs were synthesized using the Ambion mMessage mMachine T7 transcription kit (Thermo Fisher Scientific) and kept at 1 µg/µL at −80 °C.

Females *Xenopus lævis* were anesthetized using 0.1 % Tricaine methanesulfonate (MS222, SIGMA) disolved in 0.1 % $NaHCO_3$ and maintained on ice. Defolliculated oocytes were harvested from ovaries by shaking incubation in Ca^{2+}-free OR-2 solution (in mM: 85 NaCl, 1 $MgCl_2$, 5 Hepes, pH 7.6 with KOH) containing 5 mg mL^{-1} (type A, ROCHE). Oocytes were kept at 19 °C in a Barth's solution (in mM: 88 NaCl, 1 KCl, 0.41 $CaCl_2$, 0.82 $MgSO_4$, 2.5 $NaHCO_3$, 0.33 $CaNO_3$, 5 Hepes, pH 7.4 (with NaOH)) containing 50 µg/mL gentamycin. cRNAs (50 ng) were injected using a nanoliter injector (World Precision Instruments).

Sequences alignment and phylogenetic tree

The phylogeny of SLC6 transporters in ***Figure 1***A includes 63 vertebrates orthologs of *SLC6A7*, *SLC6A9*, *SLC6A5* and *SLC6A14* from cartilaginous fishes (*Callorhinchus milii* [9, 5, 14], *Rhincodon typus* [9], bony fishes (*Danio rerio* [9, 5, 14], *Oncorhynchus mykiss* [9, 14], *Lepisosteus oculatus* [7], *Hippocampus comes* [9, 5], *Nothobranchius furzeri* [9, 5, 14]), *Latimeria chalumnae* [5], amphibians (*Nanorana parkeri* [7, 5, 14], *Xenopus lævis* [9, 5], *Xenopus tropicalis* [7, 14]), reptiles (*Chelonia mydas* [7, 9, 5, 14], *Gekko japonicus* [7, 9, 5, 14], *Notechis scutatus* [7, 5, 14]), birds (*Serinus canaria* [7, 9, 5, 14], *Empidonax traillii* [7, 9, 14], *Apteryx rowi* [7, 5, 14], *Gallus gallus* [7, 9, 14]), mammals (*Monodelphis domestica* [7, 9, 5, 14], *Mus musculus* [1, 2, 3, 4, 5, 6, 7, 8, 9, 11, 12, 13, 14], *Macaca macaca* [7, 9, 14], *Macaca menestrina* [5], *Homo sapiens* [7, 9, 5, 14]) and was generated by PhyML on phylogeny.fr (https://www.phylogeny.fr/,(***Dereeper et al., 2008***)). The tree was created and color coded using iTol (https://itol.embl.de, (***Letunic and Bork, 2007***)). The sequence alignment of ***Figure 1–Figure Supplement 2*** was produced using PROMALS3D (http://prodata.swmed.edu/promals3d/promals3d.php). Area-proportional Venn diagrams were drawn with eulerAPE software (http://www.eulerdiagrams.org/eulerAPE/,***Michalec et al.*** (***2014***)).

Electrophysiology

We used O725C amplifier (Warner Instrument) for two-electrode voltage-clamp recordings in *Xenopus* oocytes. Glass electrodes filled with 3 M KCl solution had a typical resistance of 1 MΩ. Experiments were performed at room temperature with oocytes perfused continuously with a solution containing (in mM): 100 NaCl, 1.8 $CaCl_2$, 1 $MgCl_2$, 5 Hepes, pH 7.2 (with KOH). For intracellular microinjections, oocytes were impaled with a third micropipette connected to a nanoliter injector (World Precision Instruments) and injected with small volumes (range: 13–69 nL) of concentrated glycine and NaCl. Stationary currents were digitally filtered at 10 Hz and acquired at 100 Hz using a 1320 digidata (Molecular devices). Presteady-state currents were evoked by short voltage steps 200–400 ms in the range 110–−150 mV by decrements of 10 mV. Currents were typically filtered at 1–2 kHz and digitized at 2.5–10 kHz, except for a subset of experiments where the first millisecond of the relaxation currents were precisely isolated by recording the full range of the oocyte capacitive currents at 20–50 kHz sampling frequency and filter accordingly at 4–10 kHz). Transporter currents were isolated by subtraction of traces recorded in the presence of their specific inhibitors (GlyT1: 20 µM OR24598; GlyT2: 10 µM ORG25543; $ATB^{0,+}$: 0.5–1 mM α-MT).

Ionic coupling

Oocytes expressing $ATB^{0,+}$ were voltage-clamped at −40 mV and perfused with a solution containing 30 µM glycine [U-^{14}C] (specific activity 3.81 MBq µmol^{-1}, Amersham Pharmacia Biotech) and 20 µM unlabeled glycine. After 30–120 s application and complete wash-out, unclamped oocytes were washed 3 times with ice-cold solution and lysed in 0.5 mL triton (2 %). The radioactivity was counted with a Kontron Betamatic and the charge coupling (z_T) was calculated from the slope of the relationship between glycine uptake (U_{Gly}) and the time integral of the glycine evoked current (Q_{Gly}) (***Roux and Supplisson, 2000***).

Chemicals

Chemicals were obtained from SIGMA Aldrich. ORG25543 and 0RG24598 were generous gift from Organon. We used choline$^+$ or Tris$^+$ (2-amino-2-hydroxymethyl-1,3-propanediaol) and gluconate$^-$ or methyl-sulfonate$^-$ as substitutes for Na^+ and Cl^-, respectively.

Fit procedures

The slope and saturation of the *Q-V*s depend on the apparent charge z_{max} expressed in elementary charge (*e*), and the maximal charge Q_{max} expressed in nC is proportional to the number of transporters (Tn) :

$$Q_{max} = z_{max}\,\mathrm{Tn} \tag{1}$$

Transporter *Q-V*s in ***Figure 3*** are fitted with a Boltzmann equation (2) to extract $Q_{\max}$, $z_{\max}$ and the half-distribution potential $V_{1/2}$ (***Bezanilla and Villalba-Galea, 2013***):

$$Q(V) = \frac{Q_{\max}}{1 + \exp\left[\frac{z_{\max}(V_{1/2} - V)}{kT}\right]} \tag{2}$$

k is the Boltzmann constant, and T the absolute temperature.

In the ***Figure 6***C, sets of four *Q-V*s were measured at different Na^+ concentrations for each oocyte, and then normalized by $Q_{\max}$ at [Na^+] =100 mM using equation (2) . The data set for $ATB^{0,+}$ consists of n = 1512 samples (14 oocytes x 4 *Q-V*@[Na^+] /oocyte x 27 voltages/*Q-V*), and n=513 samples for GlyT2 (7 oocytes x 4 *Q-V*@[Na^+] /oocyte x 19 voltages/*Q-V*; one *Q-V*@Na^+ = 10 mM was excluded because of a subtraction artifact). Concentrations of Na^+ were not identical for both transporters for no particular purpose. A global fit of each data set as function of Na^+ and voltage was performed using the equilibrium equations of schemes #1, #2, and #3 that are detailed in***Figure 6–Figure Supplement 1***B, using the NonLinearFitModel function in Mathematica 12 (Wolfram). The ΔAkaike values tabulated in ***Figure 6–Figure Supplement 1***B are the Akaike values given by Mathematica after subtraction of the minimum value for the scheme #1. The RSquared of model #3 were 0.991 and 0.990 for $ATB^{0,+}$ and GlyT2, respectively.

In the scheme #3, $z_{\max}$ is not constant for $ATB^{0,+}$ because $z_\gamma > z_\alpha + z_\beta$. We computed $z_{\max}$ as function of Na^+ in***Figure 6***D, using the probability (***Zifarelli et al., 2012***) of Na^+-unbound states ($p(U^c)$, $p(U)$) and Na^+-bound states ($p(B)$, $p(B^c)$) as shown in***Figure 6–Figure Supplement 4***:

$$z_{max} = -z_\alpha(p(U(V_{\max})) - p(U(V_{\min})) - (z_\alpha + z_\beta)(p(B(V_{\max})) - p(B(V_{\min})) - (z_\alpha + z_\beta - z_\gamma)(p(B^c(V_{\max})) - p(B^c(V_{\min}))$$

$$\text{with} \quad \left| \begin{array}{ll} p(U(V_{\min})) = 0 & p(U(V_{\max})) = 0 \\ p(B(V_{\min})) = 1 & p(B(V_{\max})) = 0 \\ p(B^c(V_{\min})) = 0 & p(B^c(V_{\max})) = x \end{array} \right.$$

$$z_{max} = (z_\alpha + z_\beta)(1 - x) + z_\gamma\, x \tag{3}$$

The median voltage for activation ($V_{\text{med.}}$) corresponds to the voltage for equal negative and positive integrals of the *Q-V* (***Figure 6–Figure Supplement 5***) :

$$\int_{V_{\min}}^{V_{\text{med.}}} Q(V)dV = \int_{V_{\text{med.}}}^{V_{\max}} Q(V_{\max}) - Q(V)dV. \tag{4}$$

$V_{\text{med.}}$ is estimated using the FindRoot and Nintegrate functions of Mathematica 12.

To simulate the time course of the relaxation currents in ***Figure 6***F, we used the NDSolve function (Mathematica 12) and numerically integrates the three differential equations that defined the dynamics of the four-state model U^cUBB^c (***Figure 6–Figure Supplement 1***A):

$$\begin{aligned} \frac{dU^c}{dt} &= k21_{(V,t)}\, U - k12_{(V,t)}\, U^c \\ \frac{dU}{dt} &= k12_{(V,t)}\, U^c + k32_{(V,t)}\, B - (k21_{(V,t)} + k23_{(Na,V,t)})\, U \\ \frac{dB}{dt} &= k23_{(Na,V,t)}\, U + k43_{(V,t)}\,(1 - U^c - U - B) - (k32_{(V,t)} + k34_{(V,t)})\, B \end{aligned}$$

The individual rates are defined by the voltage-independent rates ($k12_0$, $k23_0$, $k34_0$) and constants (α_0, Kd, γ_0, see ***Figure 6–Figure Supplement 1***A) obtained from the *Q-V* fit (***Figure 6***B). The equivalent charge for each step (z_α, z_β, z_γ) are expressed in *e*, and the fraction of the membrane potential (d_α,

d_β), d_γ)) define the voltage dependency of forward and bacward reactions:

$$
\begin{aligned}
k12_{(V,t)} &= k12_0\, exp\left[-d_\alpha\, z_\alpha\, \mu\, V_t\right] \\
k21_{(V,t)} &= \frac{k12_0}{\alpha_0}\, exp\left[(1-d_\alpha)\, z_\alpha\, \mu\, V_t\right] \\
k23_{(Na,V,t)} &= k23_0\, \left[Na^+\right]^{n_H}\, exp\left[-d_\beta\, z_\beta\, \mu\, V_t\right] \\
k32_{(V,t)} &= k23_0\, Kd^{nH}\, exp\left[(1-d_\beta)\, z_\beta\, \mu\, V_t\right] \\
k34_{(V,t)} &= k34_0\, exp\left[(1-d_\gamma)\, z_\gamma\, \mu\, V_t\right] \\
k43_{(V,t)} &= \frac{k34_0}{\gamma_0}\, exp\left[-d_\gamma\, z_\gamma\, \mu\, V_t\right]
\end{aligned}
$$

with $\mu = \frac{1}{kT}$, and an exponential rise of the voltage step with a time constant τ_c= 300 μs

$$
V_t = \begin{cases} V_H \cdots \cdots t < t_0 \\ V_H + \left(V - V_H\right)\left(1 - exp\left[-\left(t - t_0\right)/\tau_c\right]\right) \cdots t \geq t_0 \end{cases}
$$

Simulations were filtered by one-order Bessel filter with cutoff frequency of 1.1154 kHz using the BesselFilterModel function of Mathematica.

Figures

Acknowledgments

The authors wish to thanks Vadivel Ganapathy for the generous gift of the mATB cDNA. Anne Le Goff, Laurine Bonet and Annick Ayon for technical help in molecular biology. Alain Péchard and Yvon Cabirou for building the oocyte chambers and the microinjection setup. We wish to thank Sebastien Santini - CNRS/AMU IGS UMR7256 for managing the Phylogeny.fr site. We thank Stéphane Dieudonné for stimulating discussions and generous support.

Additional information

Funding

We wish to thank INSERM and CNRS for their continuous support. This work has received support from La Fondation pour la Recherche Médicale grant Equipes FRM DEQ20140329498 and the program « Investissements d'Avenir » launched by the French Government and implemented by ANR with the references ANR-10-LABX-54 MEMOLIFE and ANR-11-IDEX-0001-02 PSL Research University.

Author contributions

Bastien Le Guellec, Investigation, Methodology, Data Curation, Formal Analysis; France Rousseau Investigation, Data Curation, Formal Analysis; Marion Bied, Investigation, Data Curation, Formal Analysis; Stéphane Supplisson, Conceptualization, Data Curation, Formal Analysis, Investigation, Methodology, Resources, Software, Supervision, Validation, Visualization, Writing-original draft, Writing-review & editing

Author ORCIDs

Stephane Supplisson orcid.org/0000-0002-0062-9752

Ethics

Animal experimentation: All procedures involving experimental animals were performed in accordance with the European directive 2010/63/EU on the Protection of Animals used for Scientific

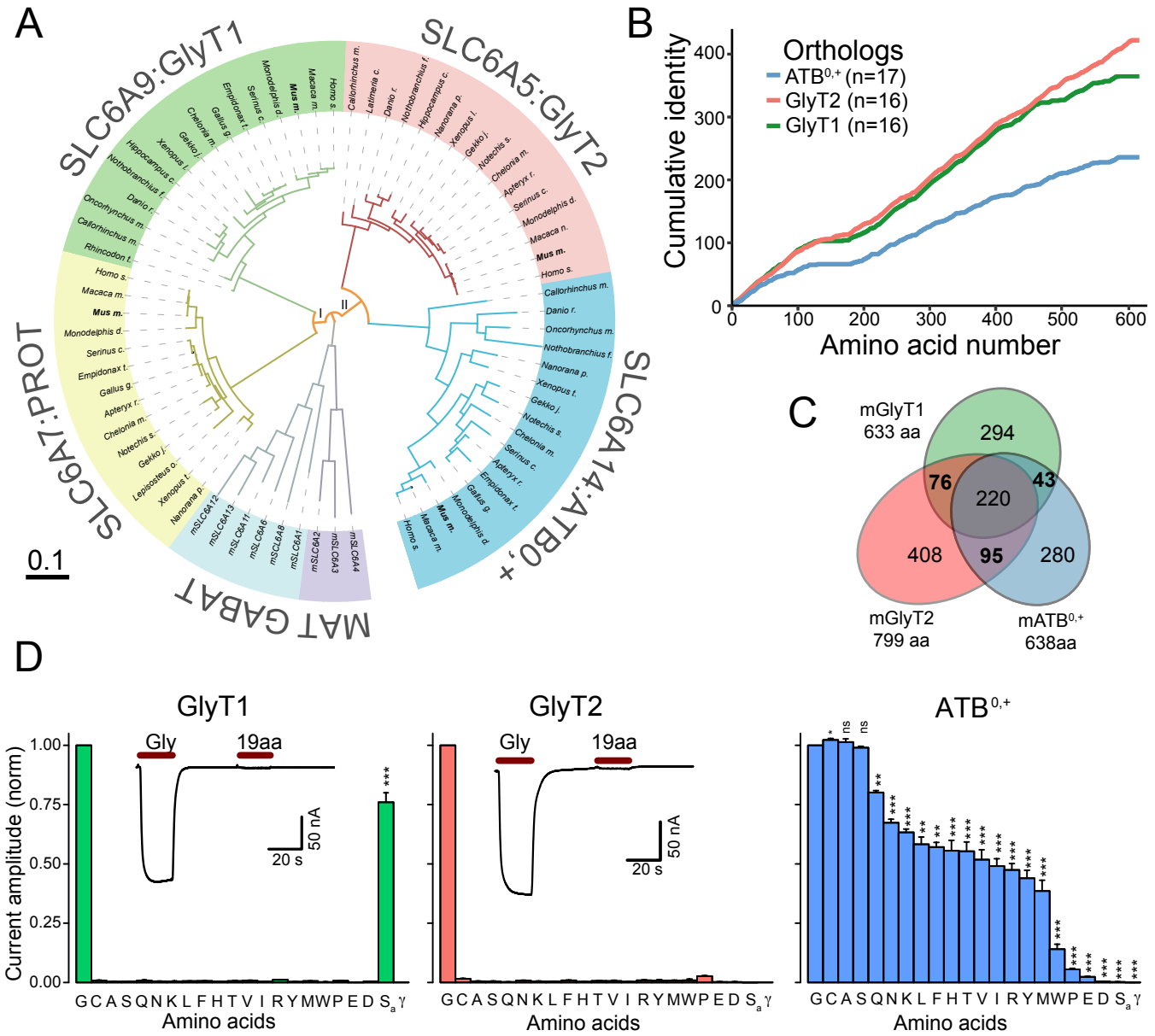

Figure 1. The divergent substrate specificity of GlyT1, GlyT2, and ATB$^{0,+}$ does not predict their phylogenetic relationship in the SLC6 family.

(A) The phylogenetic tree of amino acid transporter sequences of Vertebrates orthologs shows a split between two apparently unrelated pairs (I) PROT (n = 14) and GlyT1 (n = 16) , and (II) GlyT2 (n = 16) and ATB$^{0,+}$ (n = 17). The phylogeny includes the sequences of GABA transporters (GABAT: mGAT1 (*SLC6A1*), mTauT (*SLC6A6*), mCT1 (*SLC6A8*), mGAT3 (*SLC6A11*), mBGT1 (*SLC6A12*),and mGAT2 (*SLC6A13*), light blue) and monoamine transporters (MAT: mNET (*SLC6A2*), mDAT (*SLC6A3*), and mSERT (*SLC6A4*), purple) from *mus musculus* as outgroups. **(B)** The plot of cumulative identity for the same orthologs as in ***Figure 1***A shows that ATB$^{0,+}$ (blue, n = 17) sequences are more divergent during Vertebrates evolution than GlyT1 (green, n = 16) and GlyT2 (red, n = 16). The cumulative count (+1 if all sequences shared the same residue) starts at the first shared-position in the alignment (R57 for ATB$^{0,+}$, R309 for GlyT2 and R40 for GlyT1). **(C)** Area-proportional Venn diagrams of the number of shared and private residues for mGlyT1, mGlyT2 and mATB$^{0,+}$ based on the sequences alignment shown in ***Figure 1–Figure Supplement 2***). GlyT2 shares more identity with ATB$^{0,+}$ (n = 95) than with GlyT1 (n = 76) for all species examined ***Figure 1–Figure Supplement 1***). **(D)** Extreme divergence in substrate specificity. Individual bars represent the normalized current evoked by each amino acid in oocytes expressing GlyT1 (200 µM, n = 2-4, left panel), GlyT2 (200 µM, n = 4, middle panel) or ATB$^{0,+}$ (1 mM, n = 6-7, right panel). Amino acids are identified by their single letter code, except sarcosine (S_a) and GABA (γ). Insets show the absence of current when 19 amino acids (A,C,S,L,F,N,K,Q,H,V,T,Y,R,M,I,W,P,E,D at 200 µM are applied together compared to glycine (3.8 mM) in GlyT1-expressing oocytes (2.4 %, n = 6, p<0.001) and GlyT2-expressing oocytes (2.35 %, n=10, p=0.002). Error bars indicate SEM; paired t-test: p<0.01(***), p<0.01(**), p<0.05 (*).

Figure 1–Figure supplement 1. Sequence identities among Vertebrates orthologs of ATB$^{0,+}$, GlyT2 and GlyT1

Figure 1–Figure supplement 2. Sequences alignment of mATB$^{0,+}$, mGlyT2 and mGlyT1

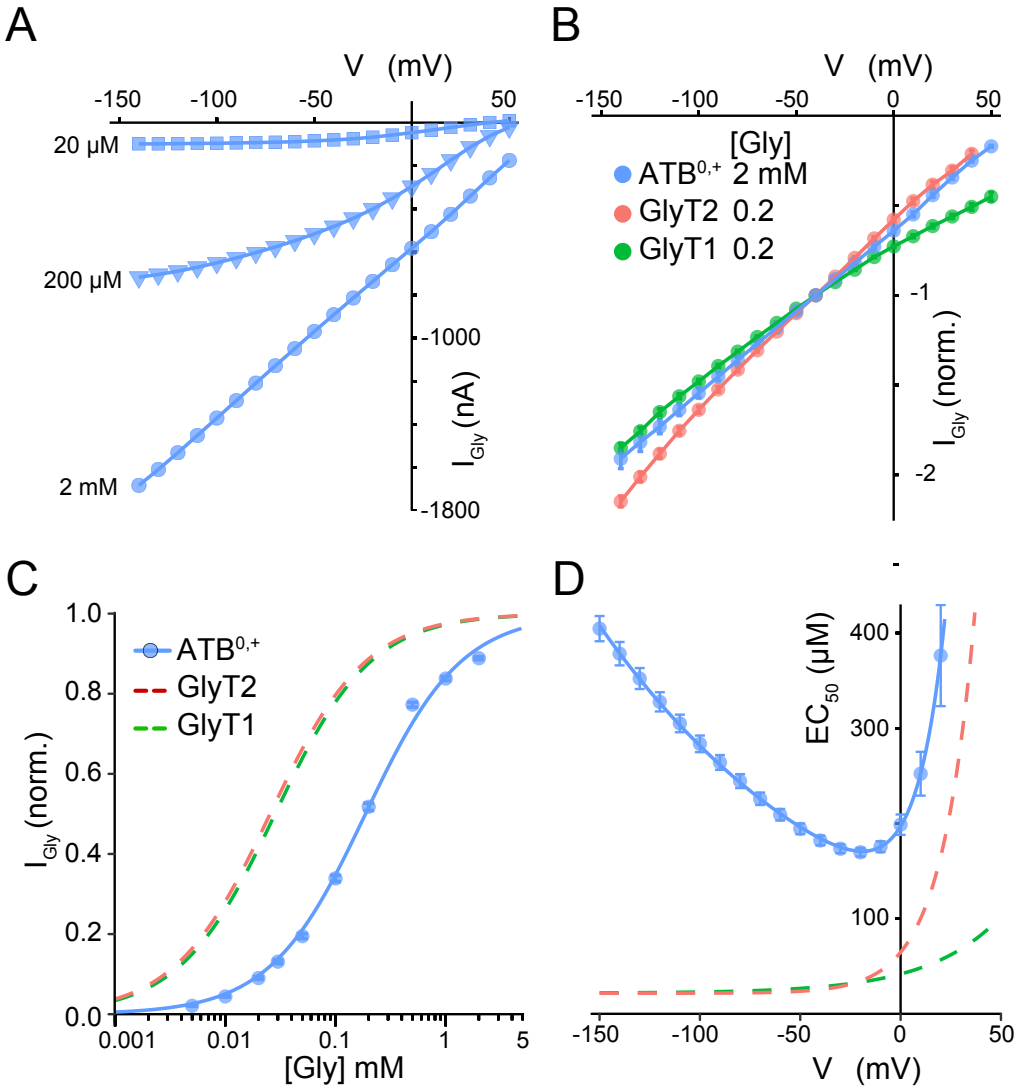

Figure 2. Weak and anomalous voltage-dependency of $ATB^{0,+}$-mediated currents

(A) Glycine evokes large inward currents in $ATB^{0,+}$-expressing oocytes. Current-voltage (I-V) relationships of the glycine-evoked current (20 µM (square), 200 µM (triangle) and 2 mM (circle)). **(B)** Linear I-Vs recorded at saturating glycine concentrations for $ATB^{0,+}$ (blue, [Gly]=2 mM, n = 10, slope = 0.92 % mV^{-1}, R^2 = 1.000, p<2 10^{16}), GlyT2 (red, [Gly]=200 µM, n = 11, slope = 1.07 % mV^{-1}, R^2 = 0.998, p<2 10^{-16}), and GlyT1 (green, [Gly]=200 µM, n = 11, slope = 0.87 % mV^{-1}, R^2 = 0.998, p = 1.78 10^{13}). Currents are normalized by the absolute amplitude at −40 mV and linear regressions were performed on the −140–−40 mV voltage range. **(C)** Glycine dose-response curve for $ATB^{0,+}$ (blue circles, V_H = −40 mV, n = 32). Individual curves were fitted by the equation: $I_{\mathrm{Gly}} = \frac{I_{\max}}{1+\frac{EC_{50}}{[Gly]_o}}$, and then normalized by the maximal amplitude ($I_{\max}$). The solid line represents the fit of the normalized equation. The glycine EC_{50} of $ATB^{0,+}$ ($EC_{50}^{ATB^{0,+}}$=189 ±5.6 µM, n=21) is higher than for GlyT1 (EC_{50}^{GlyT1} = 28 µM, green dashed line) and GlyT2 (EC_{50}^{GlyT2} = 25 µM, red dashed line) as previously determined in ***Roux and Supplisson*** (***2000***). **(D)** Anomalous voltage-dependency of $EC_{50}^{ATB^{0,+}}$ at hyperpolarized potentials (blue circles, n = 6). The solid line is the fit to the equation: $EC_{50}^{ATB0,+} = 66.2\exp(1.76\,\xi V) + 133.9\exp(-0.185\,\xi V)$. The dashed lines are fits for EC_{50}^{GlyT1} $(20.5\exp(0.7\,\xi V) + 21.7)$ and EC_{50}^{GlyT2} $(43.0\exp(1.54\,\xi V) + 21.6,\ \xi = \frac{F}{RT})$ previously determined in ***Roux and Supplisson*** (***2000***).

Figure 2–Figure supplement 1. $ATB^{0,+}$ transport current is Na^+ and Cl^--dependent

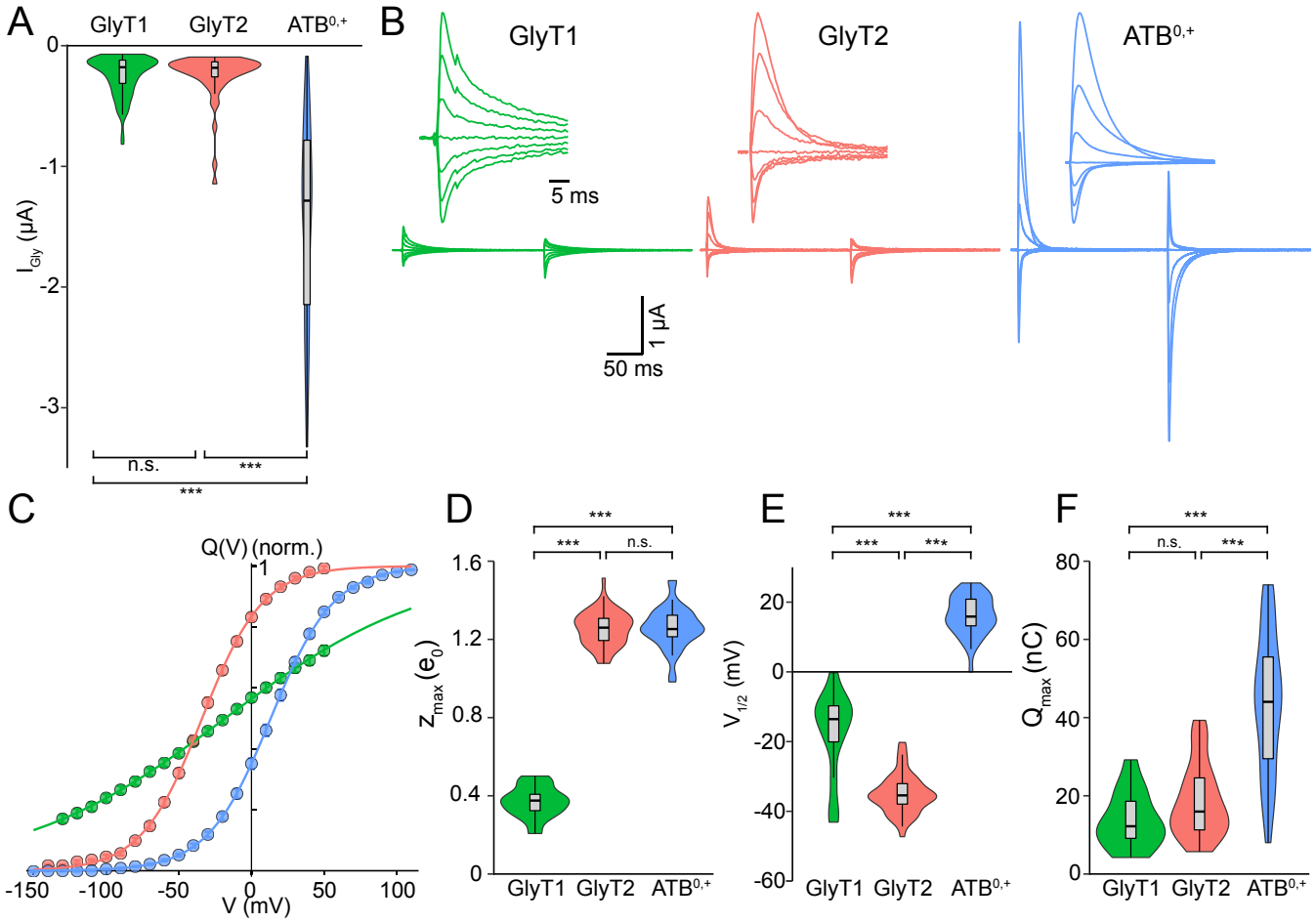

Figure 3. Presteady-state currents and the charge movement of ATB$^{0,+}$ reveals a Na^{+}-dependent convergence with GlyT2

(A) combined violin and box plots of transport current amplitudes recorded at −40 mV for different saturating glycine concentrations, that is 200 µM for GlyT1 (245.2±17.3 nA, n = 85) and GlyT2 (250.6±29.7 nA, n = 48) and 1–2 mM for ATB $^{0,+}$ (1450.0±98.8 nA, n = 65). **(B)** Representative presteady-state currents recorded in oocytes expressing GlyT1 (left, green), GlyT2 (middle, red) and ATB$^{0,+}$ (right, blue) expressing oocytes. The range of voltage steps varied from +110 mV (ATB$^{0,+}$) or +50 mV (GlyT1, GlyT2) to −150 mV by decrements of 10 mV. For clarity, only seven traces are shown, from +50 mV to −130 mV by decrements of 30 mV. Transporter currents were isolated by subtracting the traces recorded with the same voltage step protocol in the presence of specific inhibitors (10 µM ORG24598 (GlyT1); 5 µM ORG25543 (GlyT2); 1 mM α-MT (ATB$^{0,+}$)). Any residual steady-state components have been subtracted for clarity, and insets are scaled to the maximal amplitude recorded at the onset of the voltage steps. **(C)** The charge movement is the time integral of the relaxation currents plotted as a function of voltage (*Q-V*). Individual *Q-V*s for ATB$^{0,+}$ (blue, n = 38), GlyT2 (red, n = 53) and GlyT1 (green, n=15)). The solid lines are fit with a Boltzmann equation (2). **(D-F)** combined violin and box plot distributions of the Boltzmann equation parameters (D) $z_{\max}$, (E) $V_{1/2}$, and (F) $Q_{\max}$ for GlyT1 (green, n = 15), GlyT2 (red, n = 53) and ATB$^{0,+}$ (blue, n = 38).

Figure 3–Figure supplement 1. Expression of ATB$^{0,+}$ increases the linear capacitance of *Xenopus* oocytes

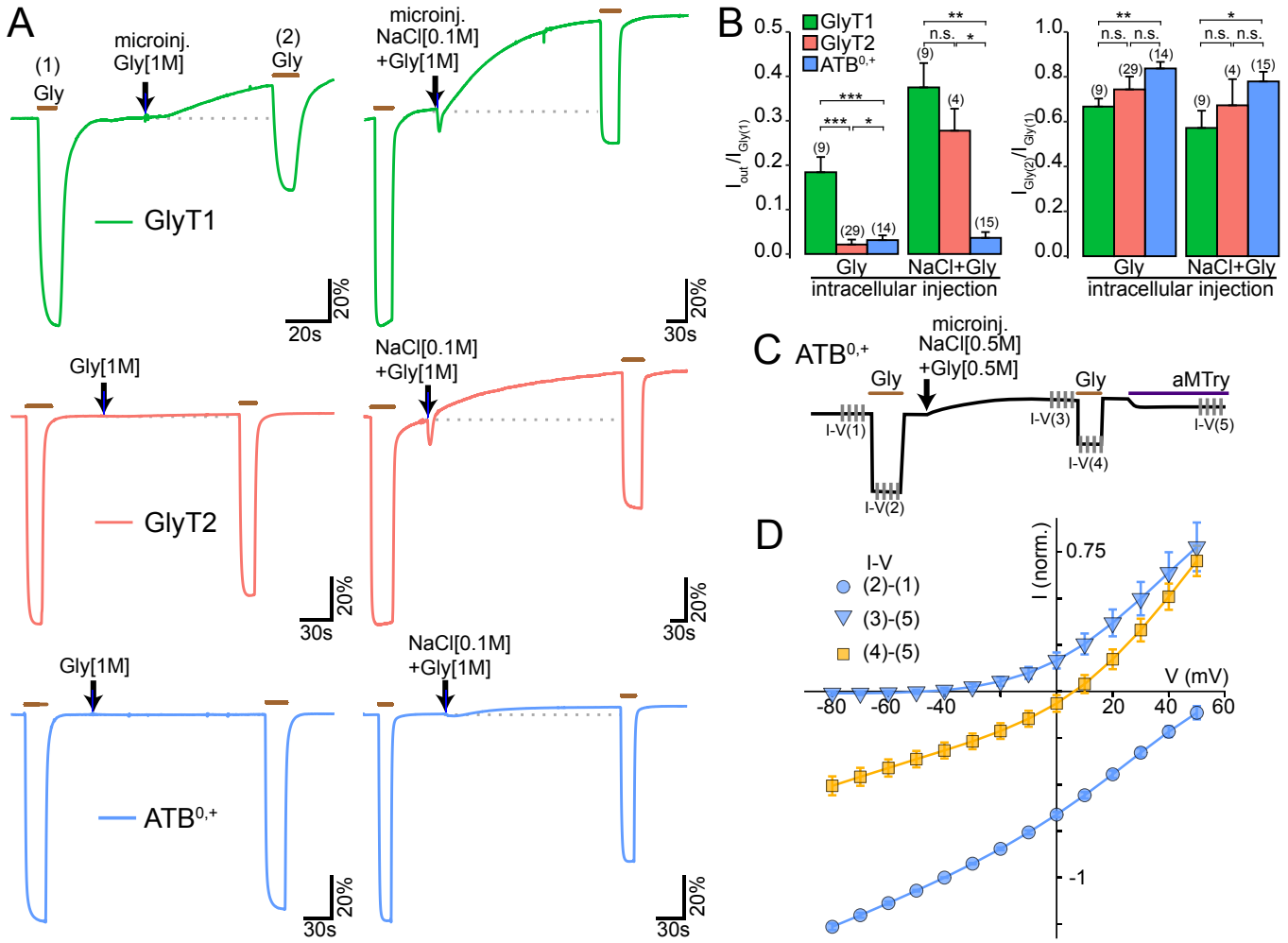

Figure 4. Microinjections of NaCl and glycine reverse $ATB^{0,+}$

(A) representatives current traces in voltage-clamp oocytes expressing GlyT1 (top trace, green), GlyT2 (middle, red) and $ATB^{0,+}$ (bottom, blue) and hold at V_H = −20 mV for two applications of glycine (200 μM before and after intracellular microinjection of a small volume solution(arrow: 20–40 nL). Left panels: microinjection of glycine (1 M) reverse GlyT1 as shown by the slow rise of an outward current (I_{out}), but not GlyT2 and $ATB^{0,+}$. Right panels: microinjection of NaCl (0.1 M) and glycine (1 M) increases I_{out} in GlyT1- and GlyT2-expressing oocytes but does not evoke robust I_{out} in $ATB^{0,+}$-expressing oocytes, while reducing the amplitude of the current for a second glycine application. Currents are normalized by the first glycine application. **(B)** Summary data for experiments in (A). The histogram show the relative amplitude of I_{out} (left) and the relative current evoked by the second glycine application (right) (mean ±SEM, n are indicated in parenthesis; *** p<0.001, **p<0.01, *p<0.05; Wilcoxon rank-sum test with Bonferroni correction for multiple comparison). **(C)** Schema of the typical protocol with five I-Vs that allow recordings of outward and inward currents for $ATB^{0,+}$ before and after microinjection of 16–20 nL of a solution containing 0.5 M NaCl and glycine. $ATB^{0,+}$-mediated currents are isolated by subtraction of the I-V recorded in the presence of α-MT (500 μM). **(D)** Normalised $ATB^{0,+}$ current-voltage relationships (IVs) for two glycine applications (200 μM) before (blue circles) and after (orange squares) 18 nL microinjection of glycine (0.5 M) and NaCl (0.5 M) that generates only outward currents (blue triangles). The IV subtractions are indicated in the legend and correspond to the five IVs described in C. Data are mean ±SEM for six oocytes. Amplitudes are normalized by the absolute amplitude of the glycine current recorded before injection at V_H =−40 mV.

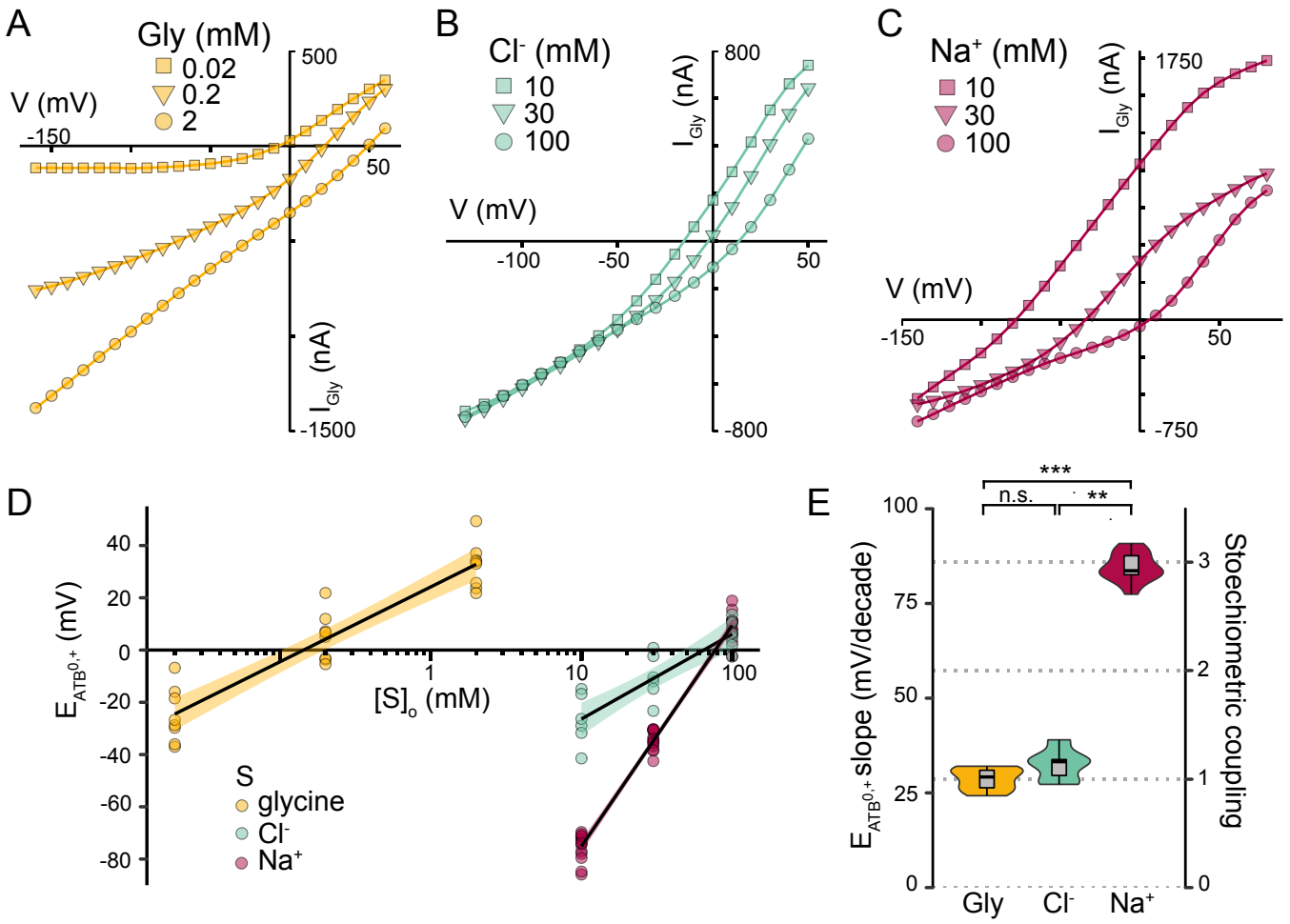

Figure 5. The reversal potential slopes method establishes a 3 Na^+/1 Cl^-/glycine stoechiometry for $ATB^{0,+}$

(A-C) shifts in reversal potentials of three I-Vs recorded in microinjected $ATB^{0,+}$-expressing oocytes (13–23 nL) of a concentrated (0.5 M) solution of NaCl + glycine) for (**(A)**) hundred-fold change in external glycine concentration or ten-fold concentration change in **(B)** Cl^- and **(C)** Na^+. Currents recorded with the same protocol in the presence of α-MT (500 µM or 1 mM at low Na^+) have been subtracted. **(D)** Semi-log plot of reversal potentials for the experiments described in A-C as function of each cosubstrate concentrations (S). Slopes of reversal potential changes were calculated for glycine (orange, $E^{Gly}_{ATB^{0,+}}$=28.6 mV/decade, R^2=0.873, p<2.47 10^{-11}, n = 8 oocytes), Cl^- (green, $E^{Cl^-}_{ATB^{0,+}}$=32.5 mV/decade, R^2=0.754, p=2.96 10^{-6}, n = 6 oocytes), and Na^+ (red, $E^{Na^+}_{ATB^{0,+}}$=84.6 mV/decade, R^2=0.983, p<2 10^{-16}, n = 14 oocytes) with the 95 % confidence interval shown in shade areas. **(E)** combined violon and box plot distributions of $ATB^{0,+}$ reversal potential slopes and stoichiometric coefficients for glycine, Cl^- and Na^+.

Figure 5–Figure supplement 1. $ATB^{0,+}$ charge-coupling and turnover rate

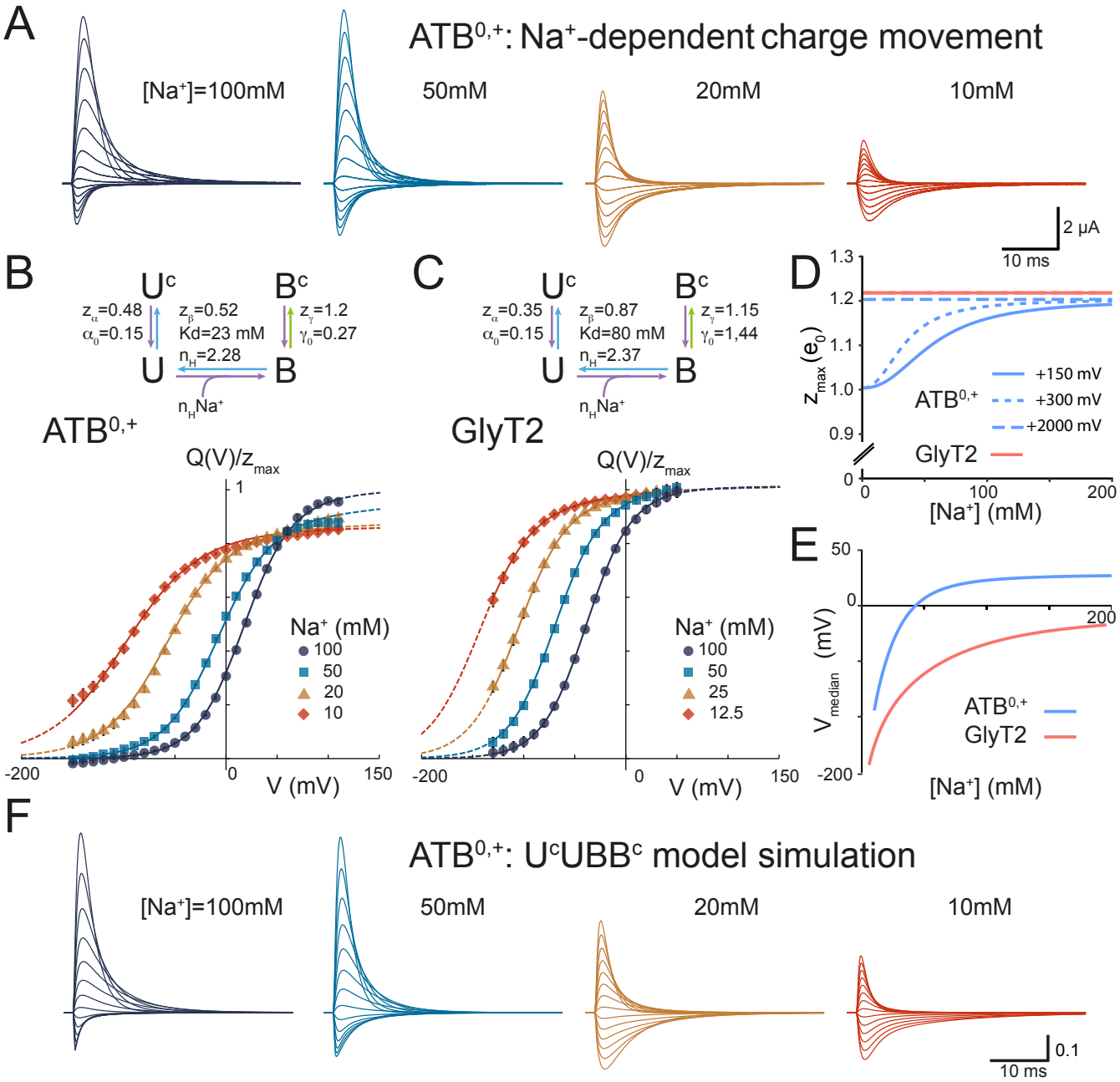

Figure 6. The charge movement shows evidence for an external gate controlling Na^+ access and locking in apo-$ATB^{0,+}$

(A) Representative traces of $ATB^{0,+}$-PSSCs recorded at the onset of voltage steps (from +110 mV to −150 mV by decrements of 20 mV; V_H = −40 mV) in glycine-free solution containing the indicated Na^+ concentration. $ATB^{0,+}$-specific PSSCs are isolated by subtraction of traces recorded in the presence of α-MT (1 mM); any residual currents have been subtracted for clarity. **(B-C)** Normalyzed *Q-Vs* for $ATB^{0,+}$ (B, n = 14, ±SEM) and GlyT2 (C, n = 7, ±SEM) for the four Na^+ concentrations shown in A, with the same color code. The data are average of sets of four *Q-Vs* normalized by the Q_{max} value for [Na^+]=100 mM. The solid lines correspond to the fit of the four-state scheme (#3) depicted above, with a gating, Na^+-binding and Na^+-locking steps that are detailed in ***Figure 6–Figure Supplement 1***. The green and blue arrows in the model represent the two steps activated during depolarization while the purple arrows identifies steps activated by hyperpolarizing voltage steps. The dashed lines of the *Q-Vs* are extrapolations of the model outside the experimental voltage range. **(D-E)** The (D) median voltage (D) and apparent charge displacement (E) plotted as function of [Na^+]. The median voltage is estimated as shown in (***Figure 6–Figure Supplement 6***). **(F)** model prediction of $ATB^{0,+}$-PSSCs for the same conditions as in A. The rate constants are described in the Materials and Methods section. The voltage independent rate constants are $k12_0$=79 s^{-1}, $k23_0$=88 mol^{-1} s^{-1} and $k34_0$=23 s^{-1}, with $d_\alpha = 0.36$, $d_\beta = 0.42$ and $d_\gamma = 0.7$. The off rate constants are back calculated using the equations, equilibrium constants and valencies detailed in ***Figure 6–Figure Supplement 1***B.

Figure 6–Figure supplement 1. A four-state sequential model for the charge movement of $ATB^{0,+}$ and GlyT2

Figure 6–Figure supplement 2. The equivalent charge displacement of $ATB^{0,+}$ is Na^+-dependent

Figure 6–Figure supplement 3. *Q-Vs* Global fits

Figure 6–Figure supplement 4. Distribution of the four states of scheme #3 at different Na^+ concentrations

Figure 6–Figure supplement 5. Q_{max} convergence at low Na^+ concentration required extreme voltage

Figure 6–Figure supplement 6. Na^+-dependency of the median voltage for *Q-Vs* of $ATB^{0,+}$ and GlyT2

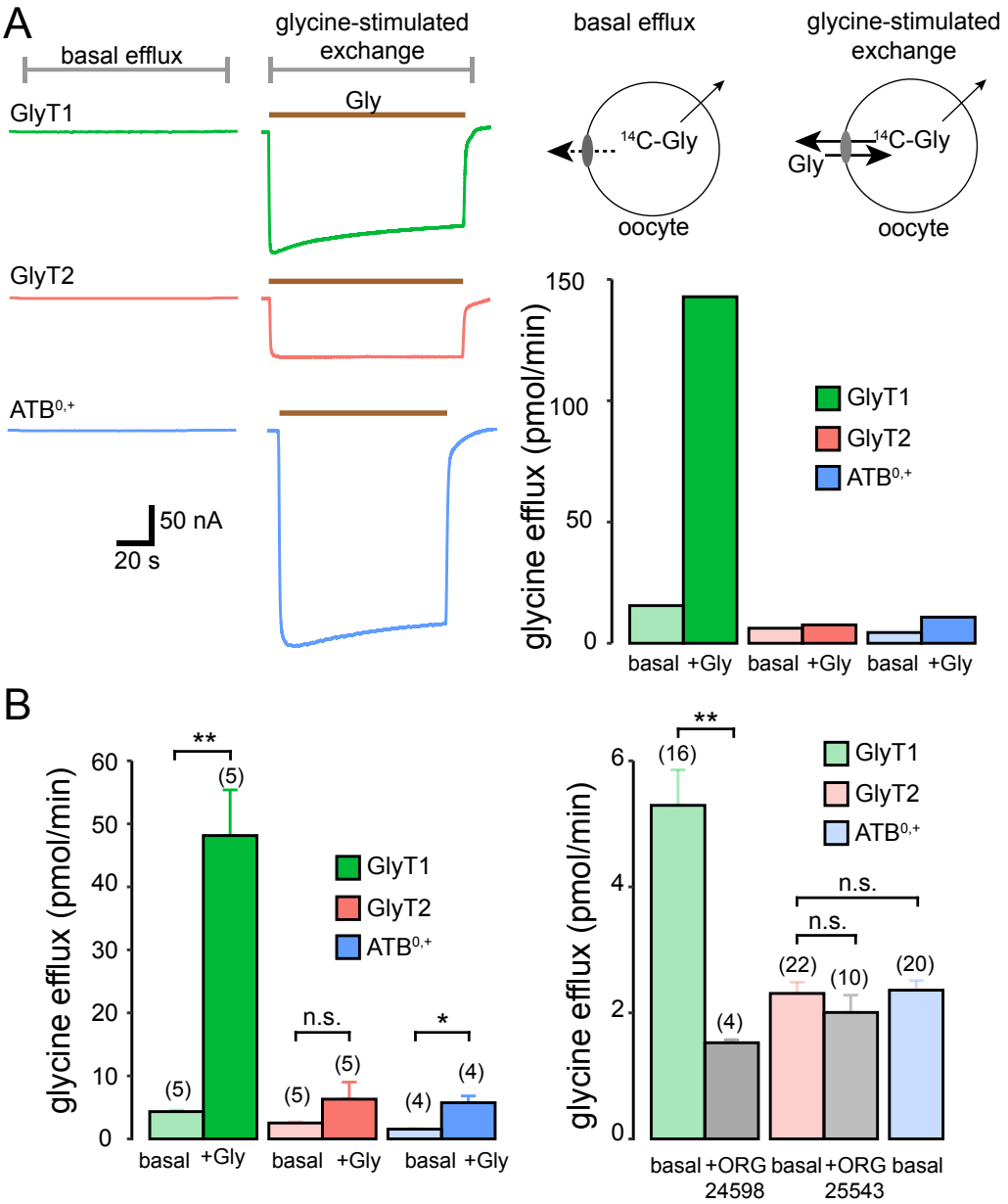

Figure 7. 3 Na^+-coupling limits glycine efflux and exchange

(A-C) extracellular glycine promotes efflux in GlyT1-expressing oocytes but not in GlyT2- and $ATB^{0,+}$-oocytes. **(A)** The efflux of glycine was measured from voltage-clamped oocytes hold at −60 mV and injected with concentrated ^{14}C-glycine. The outflow of the perfusion solution was collected for one minute in the absence (basal, left traces) or in the presence of glycine (1 mM, glycine-stimulated exchange, right traces) for oocytes expressing GlyT1 (top, green traces), GlyT2 (middle, red traces) or $ATB^{0,+}$ (bottom, blue traces). The bars histogram show glycine efflux in basal condition and during glycine application for the three transporters (same experiment). The schema shows the two components of glycine efflux in these experiments: a transporter-specific path that allow possible exchange in the presence of extracellular glycine and a non-specific component for all endogenous glycine leakage by the endogeneous transporters of *Xenopus* oocytes. **(B)** Summary data for the transtimulation of efflux (left panel) and the basal efflux (right panel). Application of OR24598 inhibits a large fraction of the basal efflux in GlyT1-expressing oocytes whereas ORG25543 has no effect, indicating minor contribution of GlyT2 to the basal glycine efflux. No inhibitor was tested with $ATB^{0,+}$ since the basal efflux was as low as GlyT2-expressing oocytes.

Purposes, the guidelines of the French Agriculture and Forestry Ministry for handling animals, and local ethics committee guidelines.

Bibliography

Ahmadi S, Wu YS, Li M, Ip W, Lloyd-Kuzik A, Paola MD, Du K, Xia S, Lew A, Bozoky Z, Forman-Kay J, Bear CE, Gonska T. Augmentation of Cystic Fibrosis Transmembrane Conductance Regulator Function in Human Bronchial Epithelial Cells via SLC6A14-Dependent Amino Acid Uptake. Implications for Treatment of Cystic Fibrosis. Am J Respir Cell Mol Biol. 2019; 61(6):755–764. doi: 10.1165/rcmb.2019-0094oc.

Ahmadi S, Xia S, Wu Y, Paola M, Kissoon R, Luk C, Lin F, Du K, Rommens J, Bear C. SLC6A14, an amino acid transporter, modifies the primary CF defect in fluid secretion. Elife. 2018; 7:e37963. doi: 10.7554/eLife.37963.

Ahmadi S, Uta M, Lauterbach A, Lipfert P, Neuhuber WL, Zeilhofer HU. Facilitation of spinal NMDA receptor currents by spillover of synaptically released glycine. Science. 2003; 300(5628):2094–2097. doi: 10.1126/science.1083970.

Amelio I, Cutruzzolá F, Antonov A, Agostini M, Melino G. Serine and glycine metabolism in cancer. Trends Biochem Sci. 2014; 39(4):191–198. doi: 10.1016/j.tibs.2014.02.004.

Anderson CM, Ganapathy V, Thwaites DT. Human solute carrier SLC6A14 is the β-alanine carrier. J Physiology. 2008; 586(Pt 17):4061–4067. doi: 10.1113/jphysiol.2008.154500.

Ankri L, Husson Z, Pietrajtis K, Proville R, Léna C, Yarom Y, Dieudonné S, Uusisaari MY. A novel inhibitory nucleo-cortical circuit controls cerebellar Golgi cell activity. eLife. 2015; 4. doi: 10.7554/elife.06262.

Apostolides PF, Trussell LO. Rapid, Activity-Independent Turnover of Vesicular Transmitter Content at a Mixed Glycine/GABA Synapse. J Neurosci. 2013; 33(11):4768–4781. doi: 10.1523/jneurosci.5555-12.2013.

Atuma C, Strugala V, Allen A, Holm L. The adherent gastrointestinal mucus gel layer: thickness and physical state in vivo. American Journal of Physiology-Gastrointestinal and Liver Physiology. 2001; 280(5):G922–G929. doi: 10.1152/ajpgi.2001.280.5.g922.

Aubrey KR, Rossi FM, Ruivo R, Alboni S, Bellenchi G, Goff A, Gasnier B, Supplisson S. The Transporters GlyT2 and VIAAT Cooperate to Determine the Vesicular Glycinergic Phenotype. J Neurosci. 2007; 27(23):6273–6281. doi: 10.1523/JNEUROSCI.1024-07.2007.

Aubrey KR, Vandenberg RJ, Clements JD. Dynamics of Forward and Reverse Transport by the Glial Glycine Transporter, Glyt1b. Biophys J. 2005; 89(3):1657–1668. doi: 10.1529/biophysj.105.061572.

Babu E, Bhutia YD, Ramachandran S, Gnanaprakasam JP, Prasad PD, Thangaraju M, Ganapathy V. Deletion of the amino acid transporter Slc6a14 suppresses tumour growth in spontaneous mouse models of breast cancer. Biochem J. 2015; 469(1):17–23. doi: 10.1042/BJ20150437.

Bail M, Martineau M, Sacchi S, Yatsenko N, Radzishevsky I, Conrod S, Ouares K, Wolosker H, Pollegioni L, Billard JM, Mothet JP. Identity of the NMDA receptor coagonist is synapse specific and developmentally regulated in the hippocampus. Proceedings of the National Academy of Sciences. 2015; 112(2):E204–E213. doi: 10.1073/pnas.1416668112.

Barilli A, Visigalli R, Ferrari F, Lascia MD, Riccardi B, Puccini P, Dall'Asta V, Rotoli BM. Organic Cation Transporters (OCTs) in EpiAirway™, a Cellular Model of Normal Human Bronchial Epithelium. Biomedicines. 2020; 8(5):127. doi: 10.3390/biomedicines8050127.

Benito-Muñoz C, Perona A, Abia D, Santos HGD, Núñez E, Aragón C, López-Corcuera B. Modification of a Putative Third Sodium Site in the Glycine Transporter GlyT2 Influences the Chloride Dependence of Substrate Transport. Frontiers in molecular neuroscience. 2018; 11:347. doi: 10.3389/fnmol.2018.00347.

Bezanilla F. How membrane proteins sense voltage. Nat Rev Mol Cell Biol. 2008; 9(4):323–332. doi: 10.1038/nrm2376.

Bezanilla F. Gating currents. The Journal of General Physiology. 2018; 150(7):911–932. doi: 10.1085/jgp.201812090.

Bezanilla F, Villalba-Galea CA. The gating charge should not be estimated by fitting a two-state model to a Q-V curve. The Journal of General Physiology. 2013; 142(6):575–578. doi: 10.1085/jgp.201311056.

Bhutia Y, Babu E, Prasad P, Ganapathy V. The amino acid transporter SLC6A14 in cancer and its potential use in chemotherapy. Asian J Pharm Sci. 2014; 9(6):293–303. doi: 10.1016/j.ajps.2014.04.004.

Bossi E, Giovannardi S, Binda F, Forlani G, Peres A. Role of anion-cation interactions on the pre-steady-state currents of the rat Na+-Cl–dependent GABA cotransporter rGAT1. The Journal of Physiology. 2002; 541(2):343–350. doi: 10.1113/jphysiol.2001.013457.

Boucher RC. Molecular insights into the physiology of the 'thin film' of airway surface liquid. The Journal of Physiology. 1999; 516(3):631–638. doi: 10.1111/j.1469-7793.1999.0631u.x.

Bröer S, Gether U. The solute carrier 6 family of transporters. Brit J Pharmacol. 2012; 167(2):256–278. doi: 10.1111/j.1476-5381.2012.01975.x.

Carta E, Chung S, James VM, Robinson A, Gill JL, Remy N, Vanbellinghen J, Drew CJ, Cagdas S, Cameron D, Cowan FM, Toro M, Graham GE, Manzur AY, Masri A, Rivera S, Scalais E, Shiang R, Sinclair K, Stuart CA, et al. Mutations in the GlyT2 Gene (SLC6A5) Are a Second Major Cause of Startle Disease. J Biol Chem. 2012; 287(34):28975–28985. doi: 10.1074/jbc.M112.372094.

Cater RJ, Vandenberg RJ, Ryan RM. Tuning the ion selectivity of glutamate transporter–associated uncoupled conductances. J Gen Physiology. 2016; 148(1):13–24. doi: 10.1085/jgp.201511556.

Chakrabarti AC. Permeability of membranes to amino acids and modified amino acids: Mechanisms involved in translocation. Amino acids. 1994; 6(3):213–29. doi: 10.1007/bf00813743.

Chatterton JE, Awobuluyi M, Premkumar LS, Takahashi H, Talantova M, Shin Y, Cui J, Tu S, Sevarino KA, Nakanishi N, Tong G, Lipton SA, Zhang D. Excitatory glycine receptors containing the NR3 family of NMDA receptor subunits. Nature. 2002; 415(6873):793. doi: 10.1038/nature715.

Chen Y, Dinges MM, Green A, Cramer SE, Larive CK, Lytle C. Absorptive transport of amino acids by the rat colon. American Journal of Physiology-Gastrointestinal and Liver Physiology. 2020; 318(1):G189–G202. doi: 10.1152/ajpgi.00277.2019.

Cherubino F, Bossi E, Miszner A, Ghezzi C, Peres A. Transient Currents in the Glycine Cotransporter GlyT1 Reveal Different Steps in Transport Mechanism. J Mol Neurosci. 2010; 41(2):243–251. doi: 10.1007/s12031-009-9281-9.

Christensen HN. Role of amino acid transport and countertransport in nutrition and metabolism. Physiological reviews. 1990; 70(1):43–77. doi: 10.1152/physrev.1990.70.1.43.

Coleman JA, Green EM, Gouaux E. X-ray structures and mechanism of the human serotonin transporter. Nature. 2016; 532:334–339. doi: 10.1038/nature17629.

Coothankandaswamy V, Cao S, Xu Y, Prasad PD, Singh PK, Reynolds CP, Yang S, Ogura J, Ganapathy V, Bhutia YD. Amino acid transporter SLC6A14 is a novel and effective drug target for pancreatic cancer. British Journal of Pharmacology. 2016; 173(23):3292–3306. doi: 10.1111/bph.13616.

Corpeleijn E, Petersen L, Holst C, Saris WH, Astrup A, Langin D, Ian M, Martinez AJ, Oppert J, Polak J, Pedersen O, Froguel P, Arner P, Sørensen T, Blaak EE. Obesity-related Polymorphisms and Their Associations With the Ability to Regulate Fat Oxidation in Obese Europeans: The NUGENOB Study. Obesity. 2010; 18(7):1369–1377. doi: 10.1038/oby.2009.377.

Corvol H, Blackman SM, Boëlle PY, Gallins PJ, Pace RG, Stonebraker JR, Accurso FJ, Clement A, Collaco JM, Dang H, Dang AT, Franca A, Gong J, Guillot L, Keenan K, Li W, Lin F, Patrone MV, Raraigh KS, Sun L, et al. Genome-wide association meta-analysis identifies five modifier loci of lung disease severity in cystic fibrosis. Nature communications. 2015; 6:8382–8390. http://dx.doi.org/10.1038/ncomms9382.

Cowgill J, Chanda B. The contribution of voltage clamp fluorometry to the understanding of channel and transporter mechanismsReview of voltage clamp fluorometry. The Journal of General Physiology. 2019; 151(10):1163–1172. doi: 10.1085/jgp.201912372.

Cui WW, Low SE, Hirata H, Louis S, Geisler R, Hume RI, Kuwada JY. The Zebrafish shocked Gene Encodes a Glycine Transporter and Is Essential for the Function of Early Neural Circuits in the CNS. J Neurosci. 2005; 25(28):6610–6620. doi: 10.1523/JNEUROSCI.5009-04.2005.

D'Argenio G, Calvani M, Casamassimi A, Petillo O, Margarucci S, Rienzo M, Peluso I, Calvani R, Ciccodicola A, Caporaso N, Peluso G, D'Argenio G, Calvani M, Casamassimi A, Petillo O, Margarucci S, Rienzo M, Peluso I, Calvani R, Ciccodicola A, et al. Experimental colitis: decreased Octn2 and Atb0+ expression in rat colonocytes induces carnitine depletion that is reversible by carnitine-loaded liposomes. The FASEB Journal. 2006; 20(14):2544–2546. doi: 10.1096/fj.06-5950fje.

Dawson KM, Collins JL, Baltz JM. Osmolarity-Dependent Glycine Accumulation Indicates a Role for Glycine as an Organic Osmolyte in Early Preimplantation Mouse Embryos. Biol Reprod. 1998; 59(2):225–232. doi: 10.1095/biolreprod59.2.225.

Dereeper A, Guignon V, Blanc G, Audic S, Buffet S, Chevenet F, Dufayard J, Guindon S, Lefort V, Lescot M, Claverie J, Gascuel O. Phylogeny.fr: robust phylogenetic analysis for the non-specialist. Nucleic Acids Res. 2008; 36(suppl_2):W465–W469. doi: 10.1093/nar/gkn180.

Drew D, Boudker O. Shared Molecular Mechanisms of Membrane Transporters. Annual Review of Biochemistry. 2015; 85(1):1–30. doi: 10.1146/annurev-biochem-060815-014520.

Eulenburg V, Retiounskaia M, Papadopoulos T, Gomeza J, Betz H. Glial glycine transporter 1 function is essential for early postnatal survival but dispensable in adult mice. Glia. 2010; 58:1066–1073. http://www.ncbi.nlm.nih.gov/pubmed/20468048.

Eulenburg V, Armsen W, Betz H, Gomeza J. Glycine transporters: essential regulators of neurotransmission. Trends Biochem Sci. 2005; 30(6):325–333. doi: 10.1016/j.tibs.2005.04.004.

Eulenburg V, Knop G, Sedmak T, Schuster S, Hauf K, Schneider J, Feigenspan A, Joachimsthaler A, Brandstätter JH. GlyT1 determines the glycinergic phenotype of amacrine cells in the mouse retina. Brain Struct Funct. 2018; 223(7):3251–3266. doi: 10.1007/s00429-018-1684-3.

Ferreira JS, Papouin T, Ladépêche L, Yao A, Langlais VC, Bouchet D, Dulong J, Mothet JP, Sacchi S, Pollegioni L, Paoletti P, Oliet SHRH, Groc L. Co-agonists differentially tune GluN2B-NMDA receptor trafficking at hippocampal synapses. Elife. 2017; 6:e25492. doi: 10.7554/eLife.25492.

Forster I, Hernando N, Biber J, Murer H. The Voltage Dependence of a Cloned Mammalian Renal Type II Na+/Pi Cotransporter (NaPi-2). The Journal of General Physiology. 1998; 112(1):1–18. doi: 10.1085/jgp.112.1.1.

Galietta LJV, Musante L, Romio L, Caruso U, Fantasia A, Gazzolo A, Romano L, Sacco O, Rossi GA, Varesio L, Zegarra-Moran O. An electrogenic amino acid transporter in the apical membrane of cultured human bronchial epithelial cells. American Journal of Physiology-Lung Cellular and Molecular Physiology. 1998; 275(5):L917–L923. doi: 10.1152/ajplung.1998.275.5.l917.

Gomeza J, Ohno K, Hülsmann S, Armsen W, Eulenburg V, Richter DW, Laube B, Betz H. Deletion of the Mouse Glycine Transporter 2 Results in a Hyperekplexia Phenotype and Postnatal Lethality. Neuron. 2003; 40(4):797–806. doi: 10.1016/S0896-6273(03)00673-1.

Grand T, Gerges S, David M, Diana MA, Paoletti P. Unmasking GluN1/GluN3A excitatory glycine NMDA receptors. Nat Commun. 2018; 9(1):4769. doi: 10.1038/s41467-018-07236-4.

Grewer C, Gameiro A, Mager T, Fendler K. Electrophysiological Characterization of Membrane Transport Proteins. Annu Rev Biophys. 2013; 42(1):95–120. doi: 10.1146/annurev-biophys-083012-130312.

Gupta N, Miyauchi S, Martindale RG, Herdman AV, Podolsky R, Miyake K, Mager S, Prasad PD, Ganapathy ME, Ganapathy V. Upregulation of the amino acid transporter ATB0,+ (SLC6A14) in colorectal cancer and metastasis in humans. Biochim Biophys Acta. 2005; 1741(1-2):215–223. doi: 10.1016/j.bbadis.2005.04.002.

Hatanaka T, Nakanishi T, Huang W, Leibach F, Prasad P, Ganapathy V, Ganapathy M. Na+ - and Cl- -coupled active transport of nitric oxide synthase inhibitors via amino acid transport system B(0,+). J Clin Invest. 2001; 107(8):1035–1043. doi: 10.1172/JCI12060.

Hatanaka T, Haramura M, Fei Y, Miyauchi S, Bridges CC, Ganapathy PS, Smith SB, Ganapathy V, Ganapathy ME. Transport of Amino Acid-Based Prodrugs by the Na+- and Cl–Coupled Amino Acid Transporter ATB0,+ and Expression of the Transporter in Tissues Amenable for Drug Delivery. J Pharmacol Exp Ther. 2004; 308(3):1138–1147. doi: 10.1124/jpet.103.057109.

Hatanaka T, Huang W, Nakanishi T, Bridges CC, Smith SB, Prasad PD, Ganapathy ME, Ganapathy V. Transport of d-Serine via the Amino Acid Transporter ATB0,+ Expressed in the Colon. Biochem Bioph Res Co. 2002; 291(2):291–295. doi: 10.1006/bbrc.2002.6441.

Hauf K, Barsch L, Bauer D, Buchert R, Armbruster A, Frauenfeld L, Grasshoff U, Eulenburg V. GlyT1 encephalopathy: Characterization of presumably disease causing GlyT1 mutations. Neurochem Int. 2020; 139:104813. doi: 10.1016/j.neuint.2020.104813.

Hilgemann DW, Lu CC. Gat1 (Gaba:Na+:Cl-) Cotransport Function. The Journal of General Physiology. 1999; 114(3):459–476. doi: 10.1085/jgp.114.3.459.

Hirata H, Carta E, Yamanaka I, Harvey RJ, Kuwada JY. Defective glycinergic synaptic transmission in zebrafish motility mutants. Front Mol Neurosci. 2010; 2:26. doi: 10.3389/neuro.02.026.2009.

Hirsch JR, Loo DDF, Wright EM. Regulation of Na+/Glucose Cotransporter Expression by Protein Kinases in Xenopus laevis Oocytes*. Journal of Biological Chemistry. 1996; 271(25):14740–14746. doi: 10.1074/jbc.271.25.14740.

Huang H, Bordey A. Glial Glutamate Transporters Limit Spillover Activation of Presynaptic NMDA Receptors and Influence Synaptic Inhibition of Purkinje Neurons. The Journal of Neuroscience. 2004; 24(25):5659–5669. doi: 10.1523/jneurosci.1338-04.2004.

Jain M, Nilsson R, Sharma S, Madhusudhan N, Kitami T, Souza AL, Kafri R, Kirschner MW, Clish CB, Mootha VK. Metabolite profiling identifies a key role for glycine in rapid cancer cell proliferation. Science. 2012; 336(6084):1040–1044. doi: 10.1126/science.1218595.

Jakobsson HE, Rodríguez-Piñeiro AM, Schütte A, Ermund A, Boysen P, Bemark M, Sommer F, Bäckhed F, Hansson GC, Johansson ME. The composition of the gut microbiota shapes the colon mucus barrier. EMBO reports. 2015; 16(2):164–177. doi: 10.15252/embr.201439263.

Jayaraman S, Song Y, Vetrivel L, Shankar L, Verkman AS. Noninvasive in vivo fluorescence measurement of airway-surface liquid depth, salt concentration, and pH. J Clin Invest. 2001; 107(3):317–324. doi: 10.1172/jci11154.

Johansson MEV, Phillipson M, Petersson J, Velcich A, Holm L, Hansson GC. The inner of the two Muc2 mucin-dependent mucus layers in colon is devoid of bacteria. Proceedings of the National Academy of Sciences. 2008; 105(39):15064–15069. doi: 10.1073/pnas.0803124105.

Johnson J, Ascher P. Glycine potentiates the NMDA response in cultured mouse brain neurons. Nature. 1987; 325(6104):529–531. doi: 10.1038/325529a0.

Karunakaran S, Ramachandran S, Coothankandaswamy V, Elangovan S, Babu E, Sudharsan P, Gurav A, Gnanaprakasam JP, Singh N, Schoenlein PV, Prasad PD, Thangaraju M, Ganapathy V. SLC6A14 (ATB0,+) protein, a highly concentrative and broad specific amino acid transporter, is a novel and effective drug target for treatment of estrogen receptor-positive breast cancer. J Biol Chem. 2011; 286(36):31830–31838. doi: 10.1074/jbc.M111.229518.

Karunakaran S, Umapathy N, Thangaraju M, Hatanaka T, Itagaki S, Munn D, Prasad P, Ganapathy V. Interaction of tryptophan derivatives with SLC6A14 (ATB0,+) reveals the potential of the transporter as a drug target for cancer chemotherapy. Biochemical Journal. 2008; 414(3):343–355. doi: 10.1042/bj20080622.

Kavanaugh MP, Bendahan A, Zerangue N, Zhang Y, Kanner BI. Mutation of an Amino Acid Residue Influencing Potassium Coupling in the Glutamate Transporter GLT-1 Induces Obligate Exchange. Journal of Biological Chemistry. 1997; 272(3):1703–1708. doi: 10.1074/jbc.272.3.1703.

Kurolap A, Armbruster A, Hershkovitz T, Hauf K, Mory A, Paperna T, Hannappel E, Tal G, Nijem Y, Sella E, Mahajnah M, Ilivitzki A, Hershkovitz D, Ekhilevitch N, Mandel H, Eulenburg V, Baris HN. Loss of Glycine Transporter 1 Causes a Subtype of Glycine Encephalopathy with Arthrogryposis and Mildly Elevated Cerebrospinal Fluid Glycine. Am J Hum Genet. 2016; 99(5):1172–1180. doi: 10.1016/j.ajhg.2016.09.004.

Legendre P. The glycinergic inhibitory synapse. Cell Mol Life Sci Cmls. 2001; 58(5):760–793. doi: 10.1007/pl00000899.

Letunic I, Bork P. Interactive Tree Of Life (iTOL): an online tool for phylogenetic tree display and annotation. Bioinformatics. 2007; 23(1):127–128. doi: 10.1093/bioinformatics/btl529.

Levy LM, Warr O, Attwell D. Stoichiometry of the Glial Glutamate Transporter GLT-1 Expressed Inducibly in a Chinese Hamster Ovary Cell Line Selected for Low Endogenous Na+-Dependent Glutamate Uptake. Journal of Neuroscience. 1998; 18(23):9620–9628. doi: 10.1523/jneurosci.18-23-09620.1998.

Li H, Limenitakis JP, Fuhrer T, Geuking MB, Lawson MA, Wyss M, Brugiroux S, Keller I, Macpherson JA, Rupp S, Stolp B, Stein JV, Stecher B, Sauer U, McCoy KD, Macpherson AJ. The outer mucus layer hosts a distinct intestinal microbial niche. Nat Commun. 2015; 6(1):8292. doi: 10.1038/ncomms9292.

Li M, Farley RA, Lester HA. An Intermediate State of the γ-Aminobutyric Acid Transporter Gat1 Revealed by Simultaneous Voltage Clamp and Fluorescence. The Journal of General Physiology. 2000; 115(4):491–508. doi: 10.1085/jgp.115.4.491.

Liu QR, López-Corcuera B, Mandiyan S, Nelson H, Nelson N. Cloning and expression of a spinal cord- and brain-specific glycine transporter with novel structural features. The Journal of biological chemistry. 1993; 268(30):22802–8. doi: 10.1016/S0021-9258(18)41598-0.

Locasale JW. Serine, glycine and one-carbon units: cancer metabolism in full circle. Nat Rev Cancer. 2013; 13(8):572–583. doi: 10.1038/nrc3557.

Loo DD, Hazama A, Supplisson S, Turk E, Wright EM. Relaxation kinetics of the Na+/glucose cotransporter. Proceedings of the National Academy of Sciences. 1993; 90(12):5767–5771. doi: 10.1073/pnas.90.12.5767.

Loo DD, Eskandari S, Boorer KJ, Sarkar HK, Wright EM. Role of Cl- in Electrogenic Na+-coupled Cotransporters GAT1 and SGLT1. J Biol Chem. 2000; 275(48):37414–37422. doi: 10.1074/jbc.M007241200.

Loo DD, Hirayama BA, Gallardo EM, Lam JT, Turk E, Wright EM. Conformational changes couple Na+ and glucose transport. Proc National Acad Sci. 1998; 95(13):7789–7794. doi: 10.1073/pnas.95.13.7789.

Lu C, Hilgemann D. GAT1 (GABA:Na+:Cl-) cotransport function. Steady state studies in giant Xenopus oocyte membrane patches. The Journal of general physiology. 1999; 114(3):429–44. doi: 10.1085/jgp.114.3.429.

Mager S, Cao Y, Lester HA. [37] Measurement of transient currents from neurotransmitter transporters expressed in Xenopus oocytes, vol. 296. sciencedirect; 1998. doi: 10.1016/S0076-6879(98)96039-6.

Mager S, Kleinberger-Doron N, Keshet GI, Davidson N, Kanner BI, Lester HA. Ion Binding and Permeation at the GABA Transporter GAT1. Journal of Neuroscience. 1996; 16(17):5405–5414. doi: 10.1523/jneurosci.16-17-05405.1996.

Mager S, Sloan J. Possible role of amino acids, peptides, and sugar transporter in protein removal and innate lung defense. Eur J Pharmacol. 2003; 479(1-3):263–267. doi: 10.1016/j.ejphar.2003.08.075.

Martina M, B -Turcotte M, Halman S, Tsai G, Tiberi M, Coyle JT, Bergeron R. Reduced glycine transporter type 1 expression leads to major changes in glutamatergic neurotransmission of CA1 hippocampal neurones in mice. The Journal of Physiology. 2005; 563(3):777–793. doi: 10.1113/jphysiol.2004.080655.

Meinild A, Loo DD, Skovstrup S, Gether U, Nanna M. Elucidating Conformational Changes in the γ-Aminobutyric Acid Transporter-1. J Biol Chem. 2009; 284(24):16226–16235. doi: 10.1074/jbc.M109.003137.

Michalec K, Mysiorek C, Kuntz M, Bérézowski V, Szczepankiewicz AA, Wilczyński GM, Cecchelli R, Nałęcz KA. Protein kinase C restricts transport of carnitine by amino acid transporter ATB0,+ apically localized in the blood–brain barrier. Archives of Biochemistry and Biophysics. 2014; 554:28–35. doi: 10.1016/j.abb.2014.05.006.

Mongeon R, Gleason MR, Masino MA, Fetcho JR, Mandel G, Brehm P, Dallman JE. Synaptic Homeostasis in a Zebrafish Glial Glycine Transporter Mutant. J Neurophysiol. 2008; 100(4):1716–1723. doi: 10.1152/jn.90596.2008.

Nakanishi T, Hatanaka T, Huang W, Prasad PD, Leibach FH, Ganapathy ME, Ganapathy V. Rapid Report. The Journal of Physiology. 2001; 532(2):297–304. doi: 10.1111/j.1469-7793.2001.0297f.x.

Noveski P, Mircevska M, Plaseski T, Peterlin B, D P. Study of Three Single Nucleotide Polymorphisms in the SLC6A14 Gene in Association with Male Infertility. Balkan J Med Genet. 2014; 17(2):61–6. doi: 10.2478/bjmg-2014-0075.

Otsu Y, Darcq E, Pietrajtis K, Mátyás F, Schwartz E, Bessaih T, Gerges SA, Rousseau CV, Grand T, Dieudonne S, Paoletti P, Acsády L, Agulhon C, Kieffer BL, Diana MA. Control of aversion by glycine-gated GluN1/GluN3A NMDA receptors in the adult medial habenula. Science. 2019; 366(6462):250–254. doi: 10.1126/science.aax1522.

Paola MD, Park AJ, Ahmadi S, Roach EJ, Wu YS, Struder-Kypke M, Lam JS, Bear CE, Khursigara CM. SLC6A14 Is a Genetic Modifier of Cystic Fibrosis That Regulates Pseudomonas aeruginosa Attachment to Human Bronchial Epithelial Cells. mBio. 2017; 8(6):e02073–17. doi: 10.1128/mbio.02073-17.

Papouin T, Ladépêche L, Ruel J, Sacchi S, Labasque M, Hanini M, Groc L, Pollegioni L, Mothet J, Oliet S. Synaptic and Extrasynaptic NMDA Receptors Are Gated by Different Endogenous Coagonists. Cell. 2012; 150(3):633–646. doi: 10.1016/j.cell.2012.06.029.

Parent L, Supplisson S, Loo D, Wright E. Electrogenic properties of the cloned Na+/glucose cotransporter: II. A transport model under nonrapid equilibrium conditions. J Membr Biology. 1992; 125(1):63–79. doi: 10.1007/BF00235798.

Penmatsa A, Wang KH, Gouaux E. X-ray structure of dopamine transporter elucidates antidepressant mechanism. Nature. 2013; 503(7474):85–90. doi: 10.1038/nature12533.

Phillips SF. Absorption and secretion by the colon. Gastroenterology. 1969; 56(5):966–71. doi: 10.1016/s0016-5085(69)80101-0.

Rees MI, Harvey K, Pearce BR, Chung S, Duguid IC, Thomas P, Beatty S, Graham GE, Armstrong L, Shiang R, Abbott KJ, Zuberi SM, Stephenson JB, Owen MJ, Tijssen MA, van den Maagdenberg AM, Smart TG, Supplisson S, Harvey RJ. Mutations in the gene encoding GlyT2 (SLC6A5) define a presynaptic component of human startle disease. Nat Genet. 2006; 38(7):801–806. doi: 10.1038/ng1814.

Rousseau F, Aubrey KR, Supplisson S. The Glycine Transporter GlyT2 Controls the Dynamics of Synaptic Vesicle Refilling in Inhibitory Spinal Cord Neurons. The Journal of Neuroscience. 2008; 28(39):9755–9768. doi: 10.1523/jneurosci.0509-08.2008.

Roux MJ, Rodrigo M, Goff A, Beatriz L, Aragón C, Supplisson S. The Glial and the Neuronal Glycine Transporters Differ in Their Reactivity to Sulfhydryl Reagents. J Biol Chem. 2001; 276(21):17699–17705. doi: 10.1074/jbc.M009196200.

Roux MJ, Supplisson S. Neuronal and Glial Glycine Transporters Have Different Stoichiometries. Neuron. 2000; 25(2):373–383. doi: 10.1016/S0896-6273(00)80901-0.

Ruffin M, Mercier J, Calmel C, Mésinèle J, Bigot J, Sutanto EN, Kicic A, Corvol H, Guillot L. Update on SLC6A14 in lung and gastrointestinal physiology and physiopathology: focus on cystic fibrosis. Cell Mol Life Sci. 2020; 77(17):3311–3323. doi: 10.1007/s00018-020-03487-x.

Sacher A, Nelson N, Ogi JT, Wright EM, Loo DDF, Eskandari S. Presteady-State and Steady-State Kinetics and Turnover Rate of the Mouse γ-Aminobutyric Acid Transporter (mGAT3). The Journal of Membrane Biology. 2002; 190(1):57–73. doi: 10.1007/s00232-002-1024-6.

Sandle GI. Salt and water absorption in the human colon: a modern appraisal. Gut. 1998; 43(2):294. doi: 10.1136/gut.43.2.294.

Shibasaki K, Hosoi N, Kaneko R, Tominaga M, Yamada K. Glycine release from astrocytes via functional reversal of GlyT1. J Neurochem. 2017; 140(3):395–403. doi: 10.1111/jnc.13741.

Sikder MOF, Sivaprakasam S, Brown TP, Thangaraju M, Bhutia YD, Ganapathy V. SLC6A14, a Na+/Cl–coupled amino acid transporter, functions as a tumor promoter in colon and is a target for Wnt signaling. Biochem J. 2020; 477(8):1409–1425. doi: 10.1042/bcj20200099.

Sikder MOF, Yang S, Ganapathy V, Bhutia YD. The Na+/Cl–Coupled, Broad-Specific, Amino Acid Transporter SLC6A14 (ATB0,+): Emerging Roles in Multiple Diseases and Therapeutic Potential for Treatment and Diagnosis. The AAPS Journal. 2017; 20(1):12. doi: 10.1208/s12248-017-0164-7.

Sipilä ST, Spoljaric A, Virtanen MA, Hiironniemi I, Kaila K. Glycine Transporter-1 Controls Nonsynaptic Inhibitory Actions of Glycine Receptors in the Neonatal Rat Hippocampus. The Journal of Neuroscience. 2014; 34(30):10003–10009. doi: 10.1523/JNEUROSCI.0075-13.2014.

Sivaprakasam S, Sikder MOF, Ramalingam L, Kaur G, Dufour JM, Moustaid-Moussa N, Wachtel MS, Ganapathy V. SLC6A14 deficiency is linked to obesity, fatty liver, and metabolic syndrome but only under conditions of a high-fat diet. Biochimica et Biophysica Acta (BBA) - Molecular Basis of Disease. 2021; 1867(5):166087. doi: 10.1016/j.bbadis.2021.166087.

Sloan JL, Grubb BR, Mager S. Expression of the amino acid transporter ATB0+ in lung: possible role in luminal protein removal. American Journal of Physiology-Lung Cellular and Molecular Physiology. 2003; 284(1):L39–L49. doi: 10.1152/ajplung.00164.2002.

Sloan JL, Mager S. Cloning and Functional Expression of a Human Na+and Cl–dependent Neutral and Cationic Amino Acid Transporter B0+. J Biol Chem. 1999; 274(34):23740–23745. doi: 10.1074/jbc.274.34.23740.

Smith KE, Borden LA, Hartig PR, Branchek T, Weinshank RL. Cloning and expression of a glycine transporter reveal colocalization with NMDA receptors. Neuron. 1992; 8(5):927–935. doi: 10.1016/0896-6273(92)90207-t.

Sniegowski T, Korac K, Bhutia YD, Ganapathy V. SLC6A14 and SLC38A5 Drive the Glutaminolysis and Serine–Glycine–One-Carbon Pathways in Cancer. Pharmaceuticals. 2021; 14(3):216. doi: 10.3390/ph14030216.

Song Y, Thiagarajah J, Verkman AS. Sodium and Chloride Concentrations, pH, and Depth of Airway Surface Liquid in Distal Airways. The Journal of General Physiology. 2003; 122(5):511–519. doi: 10.1085/jgp.200308866.

Steeves CL, Baltz JM. Regulation of intracellular glycine as an organic osmolyte in early preimplantation mouse embryos. J Cell Physiol. 2005; 204(1):273–279. doi: 10.1002/jcp.20284.

Steeves CL, Hammer MA, Walker GB, Rae D, Stewart NA, Baltz JM. The glycine neurotransmitter transporter GLYT1 is an organic osmolyte transporter regulating cell volume in cleavage-stage embryos. Proceedings of the National Academy of Sciences. 2003; 100(24):13982–13987. doi: 10.1073/pnas.2334537100.

Subramanian N, Scopelitti AJ, Carland JE, Ryan RM, O'Mara ML, Vandenberg RJ. Identification of a 3rd Na+ Binding Site of the Glycine Transporter, GlyT2. PLoS One. 2016; 11(6):e0157583. doi: 10.1371/journal.pone.0157583.

Sun L, Rommens JM, Corvol H, Li W, Li X, Chiang TA, Lin F, Dorfman R, Busson PF, Parekh RV, Zelenika D, Blackman SM, Corey M, Doshi VK, Henderson L, Naughton KM, O'Neal WK, Pace RG, Stonebraker JR, Wood SD, et al. Multiple apical plasma membrane constituents are associated with susceptibility to meconium ileus in individuals with cystic fibrosis. Nat Genet. 2012; 44(5):562–569. doi: 10.1038/ng.2221.

Supplisson S, Bergman C. Control of NMDA Receptor Activation by a Glycine Transporter Co-Expressed in Xenopus Oocytes. J Neurosci. 1997; 17(12):4580–4590. doi: 10.1523/jneurosci.17-12-04580.1997.

Supplisson S, Roux MJ. Why glycine transporters have different stoichiometries. FEBS Letters. 2002; 529(1):93–101. doi: 10.1016/s0014-5793(02)03251-9.

Suviolahti E, Oksanen LJ, Öhman M, Cantor RM, Ridderstråle M, Tuomi T, Kaprio J, Rissanen A, Mustajoki P, Jousilahti P, Vartiainen E, Silander K, Kilpikari R, Salomaa V, Groop L, Kontula K, Peltonen L, Pajukanta P. The SLC6A14 gene shows evidence of association with obesity. J Clin Invest. 2003; 112(11):1762–72. doi: 10.1172/JCI17491.

Talbot C, Lytle C. Segregation of Na/H exchanger-3 and Cl/HCO3 exchanger SLC26A3 (DRA) in rodent cecum and colon. American Journal of Physiology-Gastrointestinal and Liver Physiology. 2010; 299(2):G358–G367. doi: 10.1152/ajpgi.00151.2010.

Thiagarajah JR, Verkman AS. Chapter 55 - Water Transport in the Gastrointestinal Tract. In: Said HM, editor. *Physiology of the Gastrointestinal Tract (Sixth Edition)*, sixth edition ed. Academic Press; 2018.p. 1249–1272. https://www.sciencedirect.com/science/article/pii/B9780128099544000554, doi: https://doi.org/10.1016/B978-0-12-809954-4.00055-4.

Tsai G, Ralph-Williams RJ, Martina M, Bergeron R, Berger-Sweeney J, Dunham KS, Jiang Z, Caine BS, Coyle JT. Gene knockout of glycine transporter 1: Characterization of the behavioral phenotype. Proc Natl Acad Sci U S A. 2004; 101(22):8485–8490. doi: 10.1073/pnas.0402662101.

Uchiyama T, Fujita T, Gukasyan HJ, Kim K, Borok Z, Crandall ED, Lee V. Functional characterization and cloning of amino acid transporter B0,+ (ATB0,+) in primary cultured rat pneumocytes. J Cell Physiol. 2008; 214(3):645–654. doi: 10.1002/jcp.21254.

Ugawa S, Sunouchi Y, Ueda T, Takahashi E, Saishin Y, Shimada S. Characterization of a mouse colonic system B0+ amino acid transporter related to amino acid absorption in colon. American Journal of Physiology-Gastrointestinal and Liver Physiology. 2001; 281(2):G365–G370. doi: 10.1152/ajpgi.2001.281.2.g365, clonage of ATB dans le colon- independent pas d'expression dans le poumon !!!

Vandenberg RJ, Shaddick K, Ju P. Molecular Basis for Substrate Discrimination by Glycine Transporters. J Biol Chem. 2007; 282(19):14447–14453. doi: 10.1074/jbc.m609158200.

Villalobos C, Núñez L, J G. Mechanisms for stimulation of rat anterior pituitary cells by arginine and other amino acids. The Journal of Physiology. 1997; 502(2):421–431. doi: 10.1111/j.1469-7793.1997.421bk.x.

Wadiche JI, Arriza JL, Amara SG, Kavanaugh MP. Kinetics of a human glutamate transporter. Neuron. 1995; 14(5):1019–1027. doi: 10.1016/0896-6273(95)90340-2.

Wadiche J, Amara S, Kavanaugh M. Ion fluxes associated with excitatory amino acid transport. Neuron. 1995; 15(3):721–8. doi: 10.1016/0896-6273(95)90159-0.

Wang W, Wu Z, Dai Z, Yang Y, Wang J, Wu G. Glycine metabolism in animals and humans: implications for nutrition and health. Amino Acids. 2013; 45(3):463–77. doi: 10.1007/s00726-013-1493-1.

Willford SL, Anderson CM, Spencer SR, Eskandari S. Evidence for a Revised Ion/Substrate Coupling Stoichiometry of GABA Transporters. The Journal of Membrane Biology. 2015; 248(4):795–810. doi: 10.1007/s00232-015-9797-6.

Winkle LJV, Christensen HN, Campione AL. Na+-dependent transport of basic, zwitterionic, and bicyclic amino acids by a broad-scope system in mouse blastocysts. The Journal of biological chemistry. 1985; 260(22):12118–23.

Yamashita A, Singh SK, Kawate T, Jin Y, Gouaux E. Crystal structure of a bacterial homologue of Na+/Cl–dependent neurotransmitter transporters. Nature. 2005; 437(7056):215–223. doi: 10.1038/nature03978.

Zafra F, Aragon C, Olivares L, Danbolt N, Gimenez C, Storm-Mathisen J. Glycine transporters are differentially expressed among CNS cells. Journal of Neuroscience. 1995; 15(5):3952–3969. doi: 10.1523/jneurosci.15-05-03952.1995.

Zeilhofer HU, Wildner H, Yévenes GE. Fast Synaptic Inhibition in Spinal Sensory Processing and Pain Control. Physiol Rev. 2012; 92(1):193–235. doi: 10.1152/physrev.00043.2010.

Zerangue N, Kavanaugh MP. Flux coupling in a neuronal glutamate transporter. Nature. 1996; 383(6601):634–637. doi: 10.1038/383634a0.

Zifarelli G, De Stefano S, Zanardi I, Pusch M. On the Mechanism of Gating Charge Movement of ClC-5, a Human Cl-/H+ Antiporter. Biophys J. 2012; 102(9):2060–2069. doi: 10.1016/j.bpj.2012.03.067.

Appendix 1

Thermodynamics of ATB$^{0,+}$

The thermodynamic equation for ATB$^{0,+}$ transport cycle is given by the sum of the electrochemical gradients for all cotransported substrates:

$$\Delta\tilde{\mu}_{\mathrm{ATB}^{0,+}} = n_{Na}\,\Delta\tilde{\mu}_{\mathrm{Na}^+} + m_{Cl}\,\Delta\tilde{\mu}_{\mathrm{Cl}^-} + \Delta\tilde{\mu}_{\mathrm{AA}^{0,+}} \tag{5}$$

where n_{Na} amd n_{Cl} are the stoichiometric factors for Na^+ and Cl^-, respectively and AA$^{0,+}$ designed any amino acid substrate of ATB$^{0,+}$. In the case of a neutral susbtrate acid such as glycine, eq (5) simplify to:

$$\begin{aligned}\Delta\tilde{\mu}_{\mathrm{ATB}^{0,+}} &= n_{Na}\left[RT\ln\left(\frac{[\mathrm{Na}^+]_i}{[\mathrm{Na}^+]_o}\right) + F\,V_m\right] + n_{Cl}\left[RT\ln\left(\frac{[\mathrm{Cl}^-]_i}{[\mathrm{Cl}^-]_o}\right) - F\,V_m\right] + RT\ln\left(\frac{[\mathrm{Gly}]_i}{[\mathrm{Gly}]_o}\right)\\ &= RT\ln\left[\left(\frac{[\mathrm{Na}^+]_i}{[\mathrm{Na}^+]_o}\right)^{n_{Na}} \times \left(\frac{[\mathrm{Cl}^-]_i}{[\mathrm{Cl}^-]_o}\right)^{n_{Cl}} \times \left(\frac{[\mathrm{Gly}]_i}{[\mathrm{Gly}]_o}\right)\right] + (n_{Na} - n_{Cl})\,F\,V_m\end{aligned}$$

where R is the universal gas constant (8.314 J mol^{-1}), T is the absolute temperature (298 °K) and F is the Faraday's constant (96 485 C mol^{-1}).
The reversal potential of ATB$^{0,+}$ $\left(E_{\mathrm{ATB}^{0,+}}\right)$ is given by:

$$E_{\mathrm{ATB}^{0,+}} = \frac{2.3\,R\,T}{(n_{Na} - n_{Cl})\,F}\log\left[\left(\frac{[\mathrm{Na}^+]_o}{[\mathrm{Na}^+]_i}\right)^{n_{Na}} \times \left(\frac{[\mathrm{Cl}^-]_o}{[\mathrm{Cl}^-]_i}\right)^{n_{Cl}} \times \left(\frac{[\mathrm{Gly}]_o}{[\mathrm{Gly}]_i}\right)\right] \tag{6}$$

The slopes of the log-linear relationships for each cosubstrate is the product of a constant $\left(a = \frac{2.301\,RT}{(n_{Na}-n_{Cl})\,F}\right)$ and the stoichiometric coefficients:

$$\left|\begin{array}{lcl} E^{\mathrm{Gly}}_{\mathrm{ATB}^{0,+}} &=& a\,\log\left([\mathrm{Gly}]_o\right) + b_{\mathrm{Gly}}\\ E^{\mathrm{Cl}}_{\mathrm{ATB}^{0,+}} &=& n_{\mathrm{Cl}}\,a\,\log\left([\mathrm{Cl}^-]_o\right) + b_{\mathrm{Cl}}\\ E^{\mathrm{Na}}_{\mathrm{ATB}^{0,+}} &=& n_{\mathrm{Na}}\,a\,\log\left([\mathrm{Na}^+]_o\right) + b_{\mathrm{Na}}\end{array}\right. \tag{7}$$

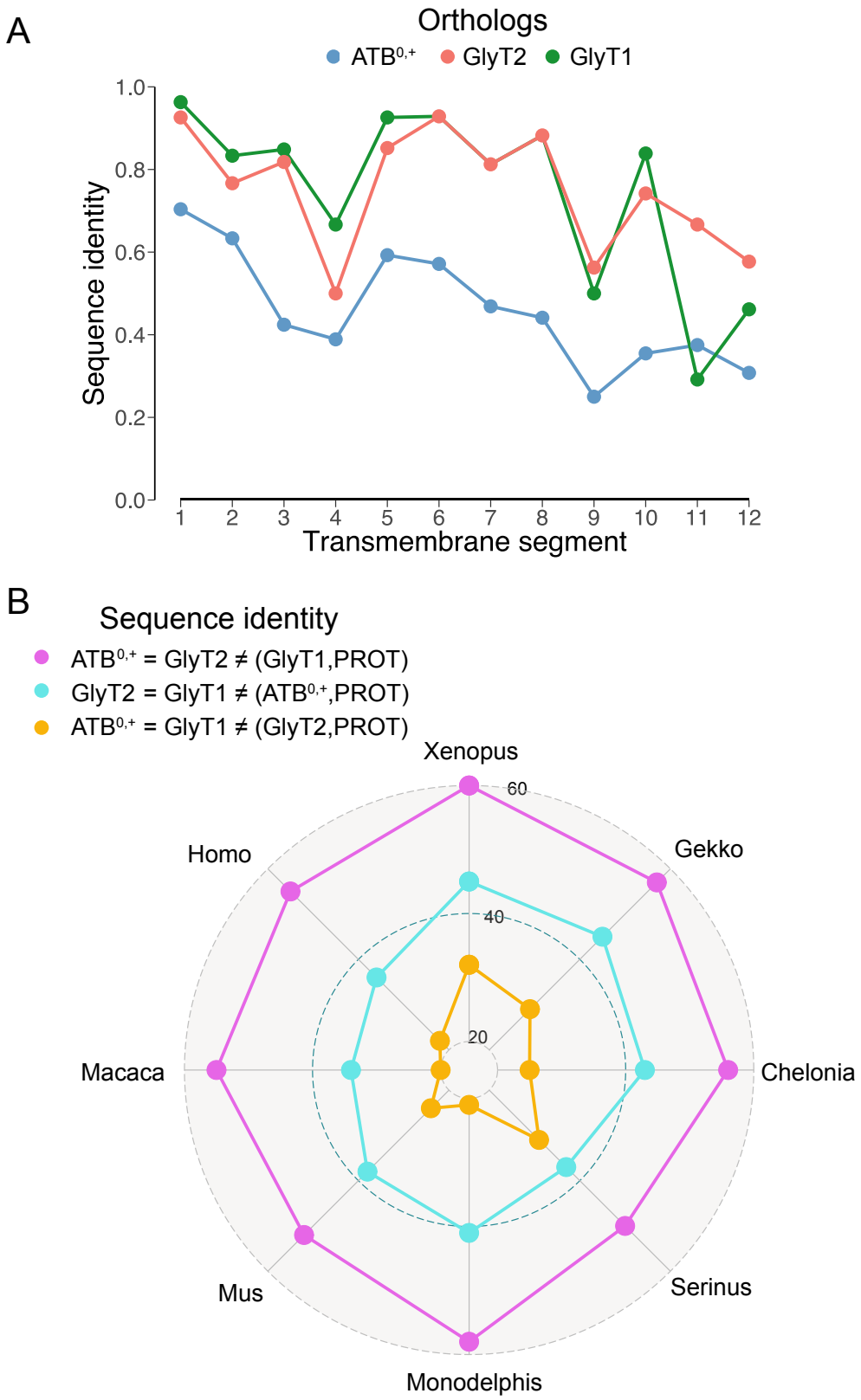

Figure 1–Figure supplement 1. **(A)** Fraction of sequence identities in the transmembrane segments (TMs) for all Vertebrates orthologs shown in **Figure 1**A, using the human SERT structure as a template for TMs delimitation(***Coleman et al., 2016***). **(B)** Radar plot of the cumulative number of sequence identity for each glycine-transporter pairs ($ATB^{0,+}$-GlyT2 (purple), GlyT2-GlyT1 (cyan), $ATB^{0,+}$-GlyT1 (yelow)). Pair identity shared with PROT are excluded as indicated in the legend

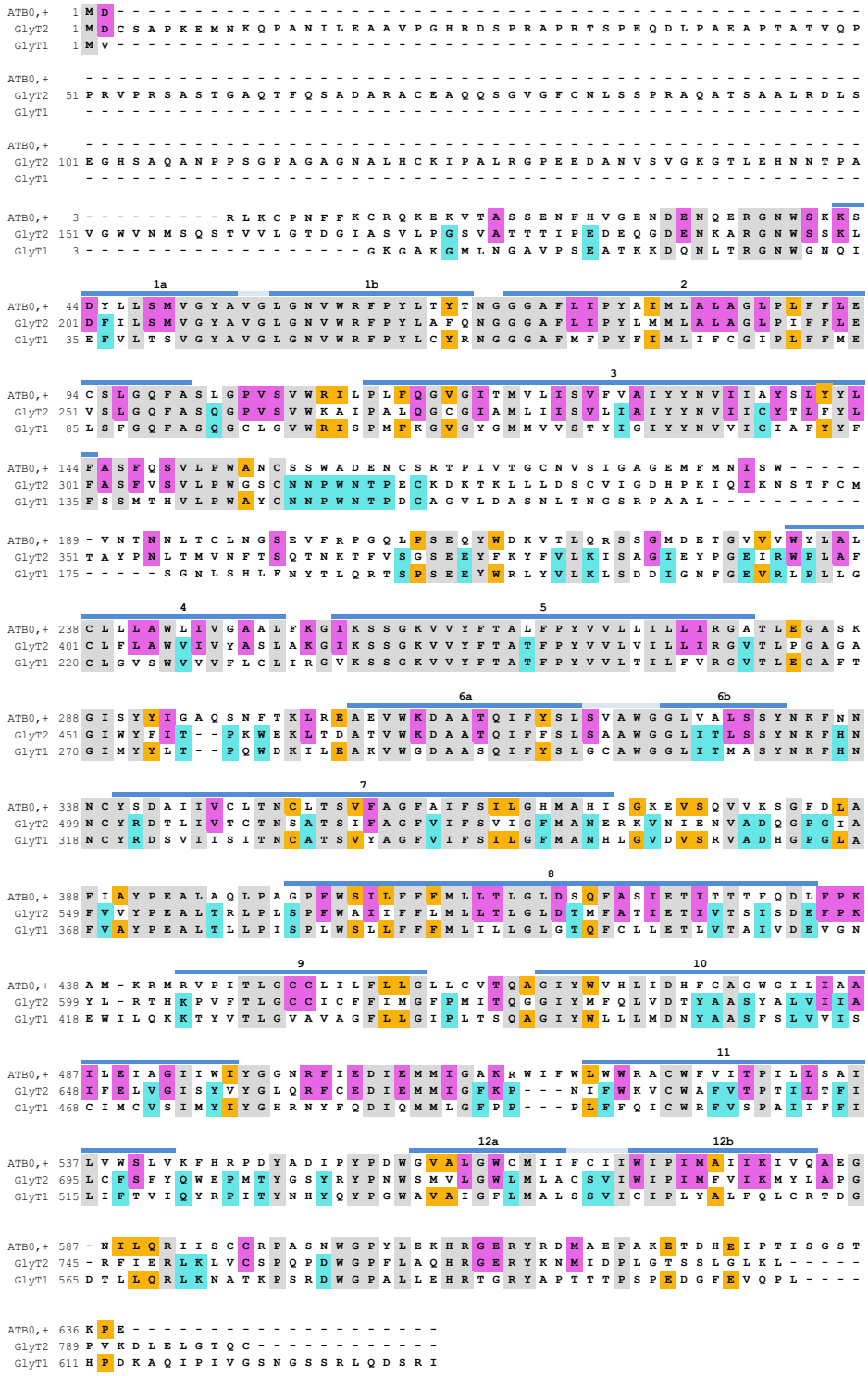

Figure 1–Figure supplement 2. Sequences alignment of the mATB$^{0,+}$, mGlyT2 and mGlyT1. The color code indicates amino acids common for the three transporters (gray, n = 220), and the identity shared between ATB$^{0,+}$ and GlyT2 (purple, n = 95), ATB$^{0,+}$ and GlyT1 (cyan, n = 43), GlyT1 and GlyT2 (orange, n = 76).

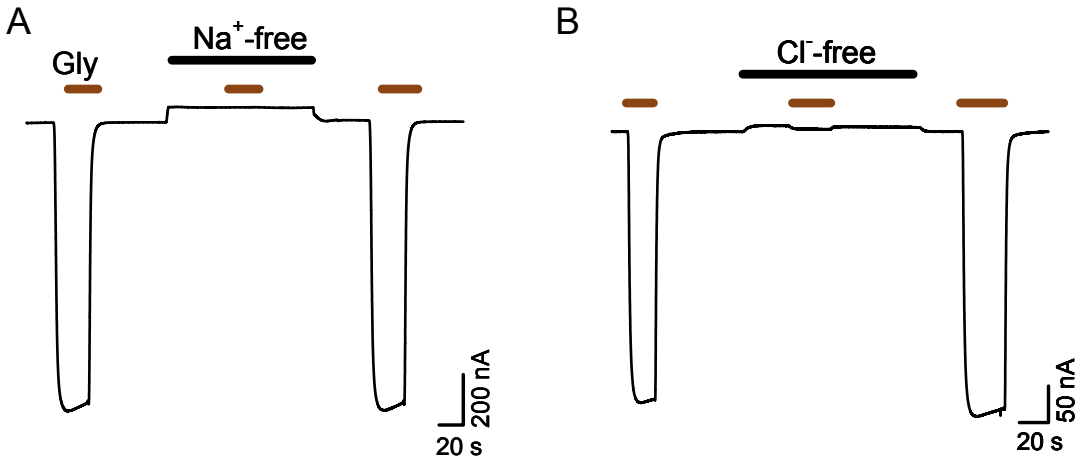

Figure 2–Figure supplement 1. Glycine evoked current in $ATB^{0,+}$-expressing oocytes is Na^+- and Cl^-- dependent (red bar: [Gly]=200 μM, V_H = −40 mV). Na^+ was substituted by choline (left trace, solid bar) and Cl^- was substituted by gluconate (right trace, solid bar).

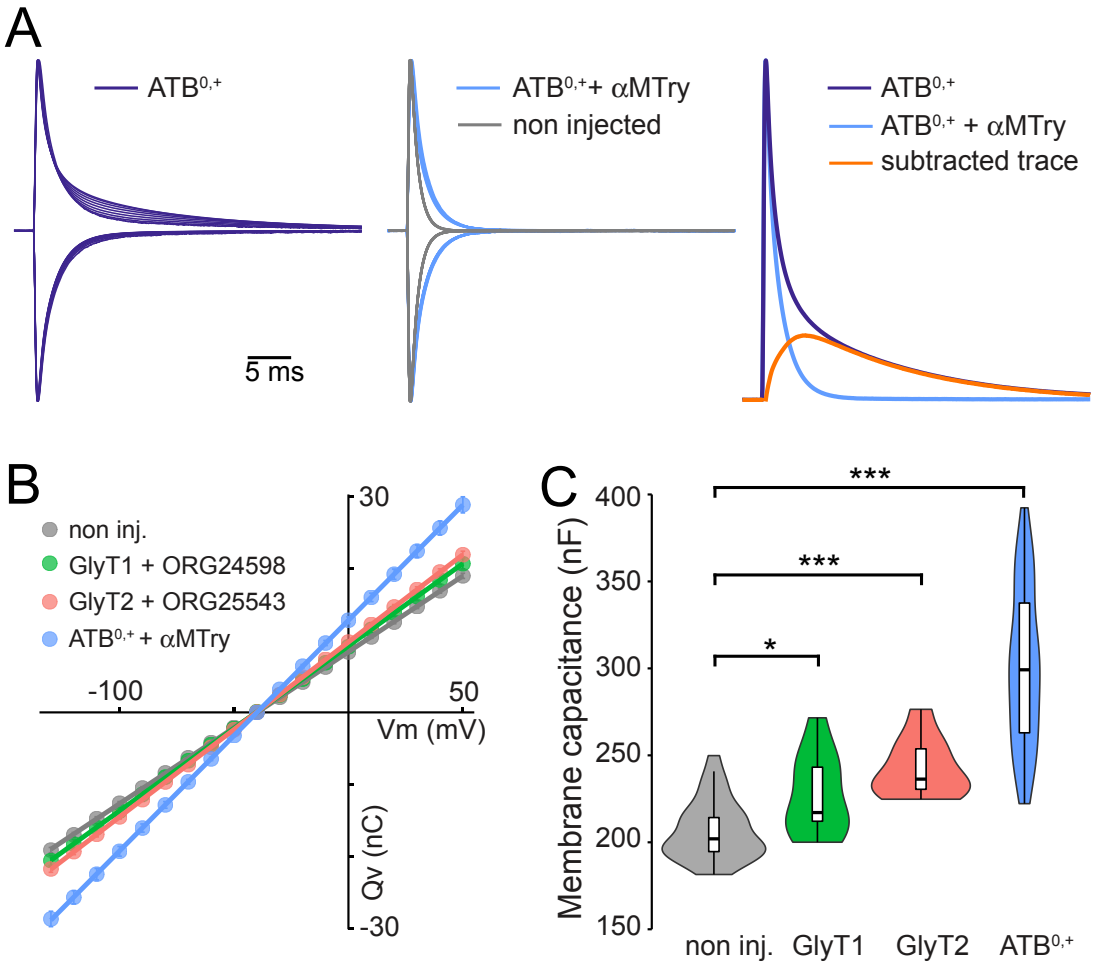

Figure 3–Figure supplement 1. **(A)** Left panel: traces of capacitive currents (linear and PSSCs) recorded at the onset of voltage steps (from +50 mV and −130 mV by decrements of 10 mV) and normalized by the peak amplitude for a representative $ATB^{0,+}$-expressing oocyte. Each trace is normalized by the absolutepeak current (the trace at V_H = −40 mV is not included). Middle panel: same as left in the presence of 1 mM α-MT (blue traces) to block $ATB^{0,+}$-charge movement. The gray traces represent currents recorded with the same protocol for a representative non injected oocyte. Right panel: the charge movement of $ATB^{0,+}$ (orange trace) for a single step at 50 mV after α-MT subtraction. **(B)** Cm is given by the slope of the linear charge-voltage relationships and increases in oocytes expressing transporter membrane capacitance (Cm) of non-injected oocytes (209±3 nF, n = 33) with oocytes expressing GlyT1+ORG24598 (227±7 nF, n = 11), GlyT2 +ORG25543 (242.8±5.2 nF, n = 10), and $ATB^{0,+}$ + α-MT320.6±11.7 nF, n = 16). **(C)** Combined violin and box plots of the distribution of linear membrane capacitance of non-injected oocytes (n = 33), and oocytes expressing GlyT1 (n = 11), GlyT2 (n = 10) and $ATB^{0,+}$ (n = 50; a group of 34 $ATB^{0,+}$-expressing oocytes was added by estimating the slope of the *Q-V* at hyperpolarized potentials).

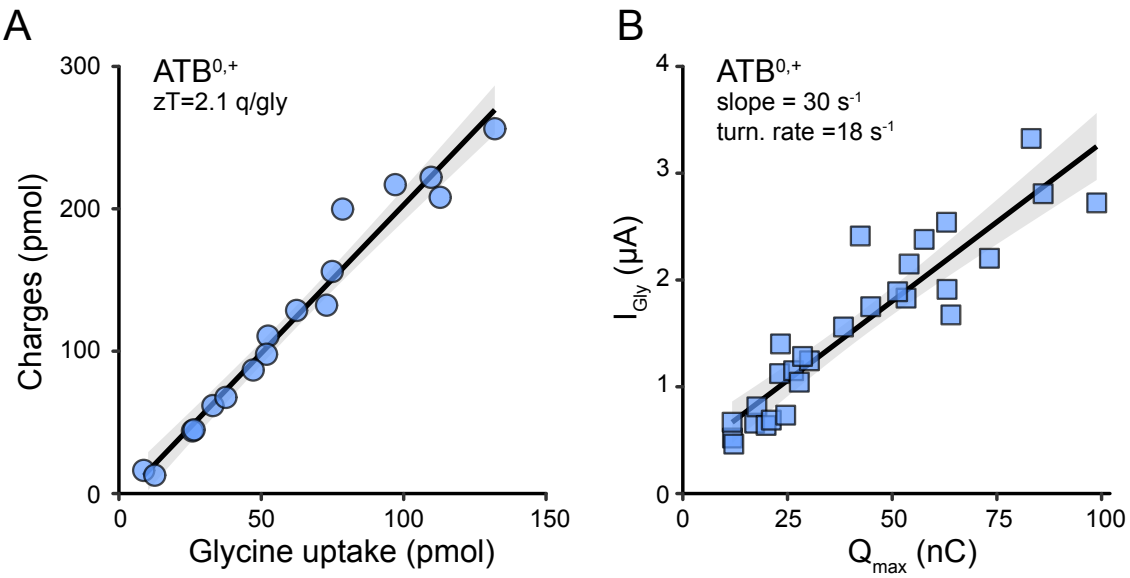

Figure 5–Figure supplement 1. **(A)** linear relationship between glycine uptake and the time integral of the glycine-evoked current for 30-120 s application of ^{14}C-glycine (50 µM, each circle represents a single oocyte expressing ATB$^{0,+}$). The slope (z_T=2.08 *e*, R^2=0.982, p=2.16 10^{-12}) gives a charge coupling per glycine in agreement with the 3 Na^+/1 Cl^- stoichiometry. The shaded area shows the 95 % confidence interval. **(B)** linear relationship between Imax ([Gly] = 1–2 mM) and $Q_{\max}$ for oocytes expressing ATB$^{0,+}$ and hold at V_H =−40 mV. An apparent turnover rate (λ=18 s^{-1}) is derived from the $I_{\max}/Q_{\max}$ slope (29.7 s^{-1}, R^2=0.848, p=3.77 10^{-12}) using the equation $\lambda = \frac{z\delta}{z_T}\frac{I_{\max}}{Q_{\max}}$, with z_T=2.08 *e* and $z\delta$=1.26 *e* as determined in A and **Figure 3**D). The shade area corresponds to the 95 % confidence interval.

A

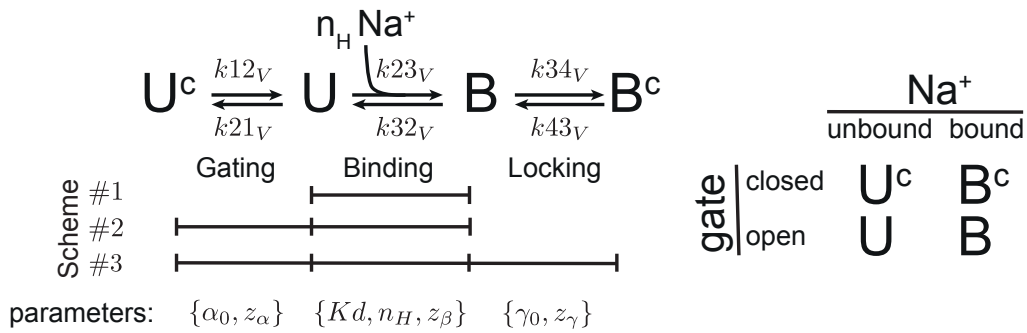

parameters: $\{\alpha_0, z_\alpha\}$ $\{Kd, n_H, z_\beta\}$ $\{\gamma_0, z_\gamma\}$

$$\alpha_V = \frac{k12_V}{k21_V} = \frac{k12_0\, e^{-z_\alpha d_\alpha \mu V}}{k21_0\, e^{z_\alpha (1-d_\alpha)\mu V}} = \alpha_0\, e^{-z_\alpha \mu V}$$

$$\beta_{Na,V} = \frac{k23_V [Na^+]^{n_H}}{k32_V} = \frac{k23_0\, [Na^+]^{n_H}\, e^{-z_\beta d_\beta \mu V}}{k32_0\, e^{z_\beta (1-d_\beta)\mu V}} = \left(\frac{[Na^+]}{Kd}\right)^{n_H} e^{-z_\beta \mu V}$$

$$\gamma_V = \frac{k34_V}{k43_V} = \frac{k34_0\, e^{z_\gamma (1-d_\gamma)\mu V}}{k43_0\, e^{-z_\gamma d_\gamma \mu V}} = \gamma_0\, e^{z_\gamma \mu V}$$

B

	Scheme		z_{max}	$\frac{Q_V}{z_{max}}$	$ATB^{0,+}$ ΔAICc	GlyT2 ΔAICc
#1	UB		z_β	$\frac{1}{1+\beta_{Na,V}}$	0	0
#2	U^CUB		$z_\alpha + z_\beta$	$\frac{1+\frac{z_\alpha}{z_{max}}\alpha_V}{1+\alpha_V(1+\beta_{Na,V})}$	-1193.5	-56.2
#3	U^CUBB^C			$\frac{z_\alpha+z_\beta(1+\alpha_V)+z_\gamma\,\alpha_V\,\beta_{Na,V}\,\gamma_V}{z_{\max}(1+\alpha_V(1+\beta_{Na,V}(1+\gamma_V)))}$		
		$z_\alpha + z_\beta \geq z_\gamma$	$z_\alpha + z_\beta$		-1757.7	-75.5
		$z_\alpha + z_\beta < z_\gamma$	z_γ		-1902.6	-75.4

Figure 6–Figure supplement 1. (A) The model shows the three kinetic schemes tested here to fit $ATB^{0,+}$- and GlyT2-*Q-V*s as function of Na^+. In glycine-free media, outward facing transporters are assumed to be either Na^+-unbound (U^c, U) or Na^+-bound (B, B^c). The UB scheme (#1) corresponds to the binary Hill model proposed by ***Mager et al.*** (***1996***) for GAT1 and is limited to a single binding step for multiple Na^+. It is defined by 3 parameters: the microscopic dissociation constant Kd, the Hill coefficient n_H, and the equivalent charge z_β. For simplicity, we define $\beta_{Na,V}$ as the equilibrium constant of the binding step as function of Na^+ and voltage. Schemes #2 and #3 include a gating step controlling the access of Na^+ to its binding sites. The equilibrium constants are α_V and γ_V for the gating and locking steps, respectively. In the scheme #2, gate closure occurs only in the unbound state (U) whereas it is independent of Na^+-binding in scheme #3. At negative potentials all transporters are in B state (***Figure 6–Figure Supplement 4***). Positive voltage steps trigger gate closure from Na^+-unbound (U) and Na^+-bound state (B). **(B)** The $z_{\max}$ and normalized *Q-V* equations are tabulated for each scheme, with the $\Delta AICc$ values estimated from the fit. $z_{\max}$ for scheme #3 is conditioned by equality or inequality of the valencies of the Na^+-release and Na^+-locking paths

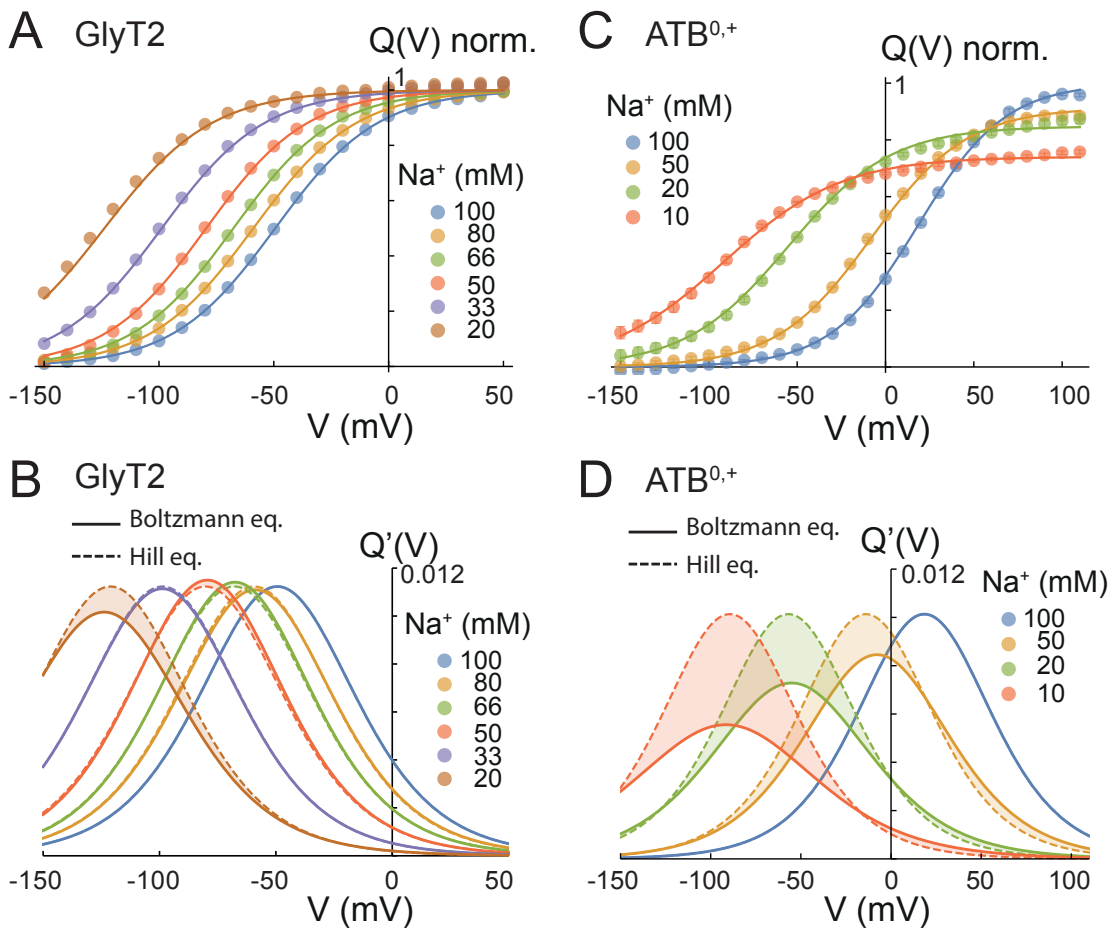

Figure 6–Figure supplement 2. (A-B) *Q-V*s for $ATB^{0,+}$ (A, n = 7) and GlyT2 (B, n = 1) for different Na^+ concentrations indicated in the legend. The solid line corresponds to the individual fit using a Boltzmann equation (**Figure 3**C). All *Q-V*s are normalized by the Q_{max} value determined for Na^+ = 100 mM . **(C-D)** The solid lines represent plots of the first derivative of the Boltzmann fits shown in A-B for $ATB^{0,+}$ (C) and GlyT2 (D). The dashed lines are the first derivative of Hill equation (scheme #1 in ***Figure 6–Figure Supplement 1***) with the parameters n= 1.9, z_{max} =0.548 and KNa= 67.4 mM for $ATB^{0,+}$ and n_H = 2.04, z_{max} =1.135 and Kd=290 mM for GlyT2

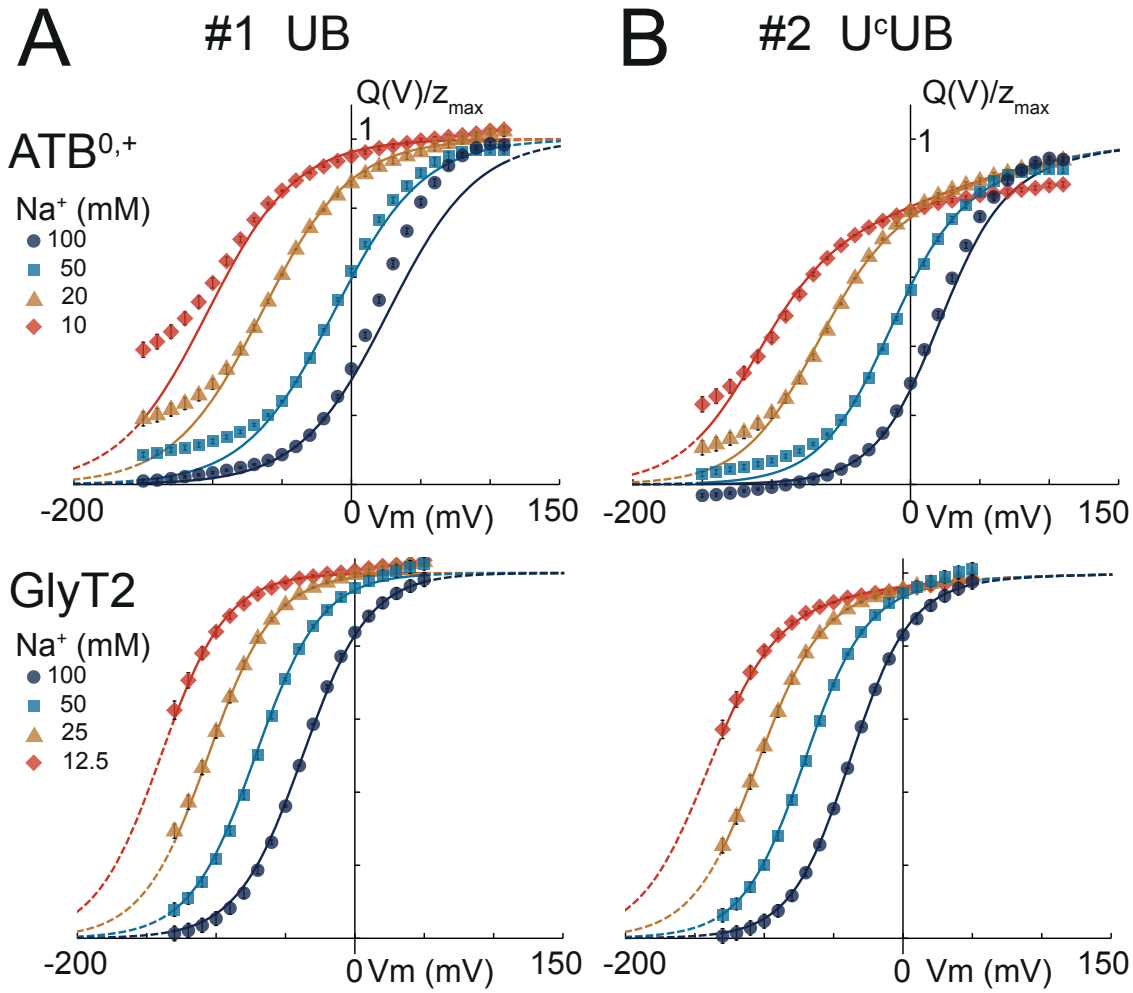

Figure 6–Figure supplement 3. (A-D) Global fits of the *Q-V*s of $ATB^{0,+}$ (top) and GlyT2 (bottom) as a function of the Na^+ concentration for the kinetic schemes #1 (A), #2 (B) as described in ***Figure 6–Figure Supplement 1***.

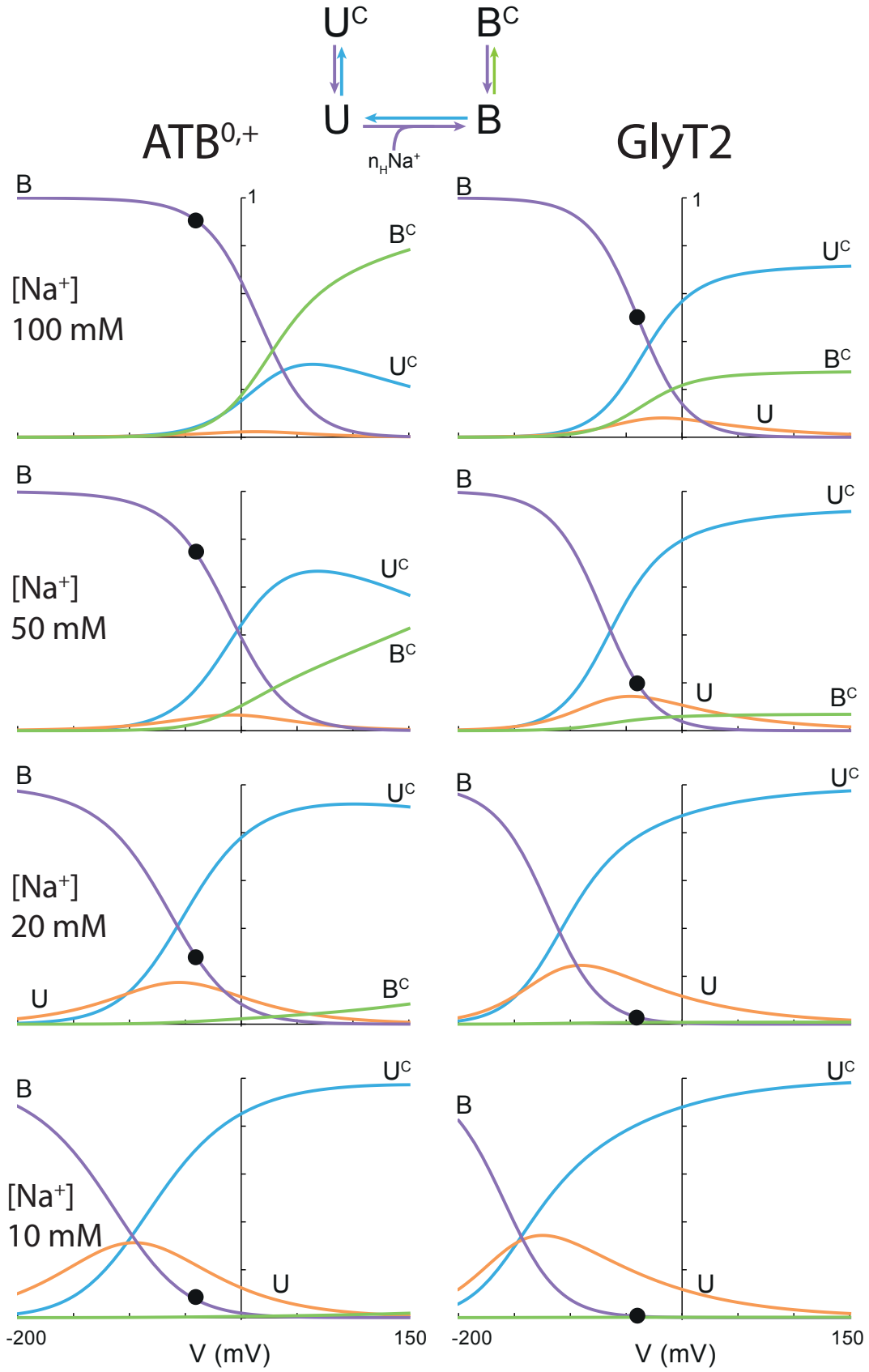

Figure 6–Figure supplement 4. The distribution of the four-state (U^c, U, B, B^c) of $ATB^{0,+}$ (left panels) and GlyT2 (right panels) plotted as a function of voltage for the Na^+ concentration indicated on the left, using the set of parameters in **Figure 6**B-C. The closed circles represent the fraction of the B state at $V_H = -40$ mV.

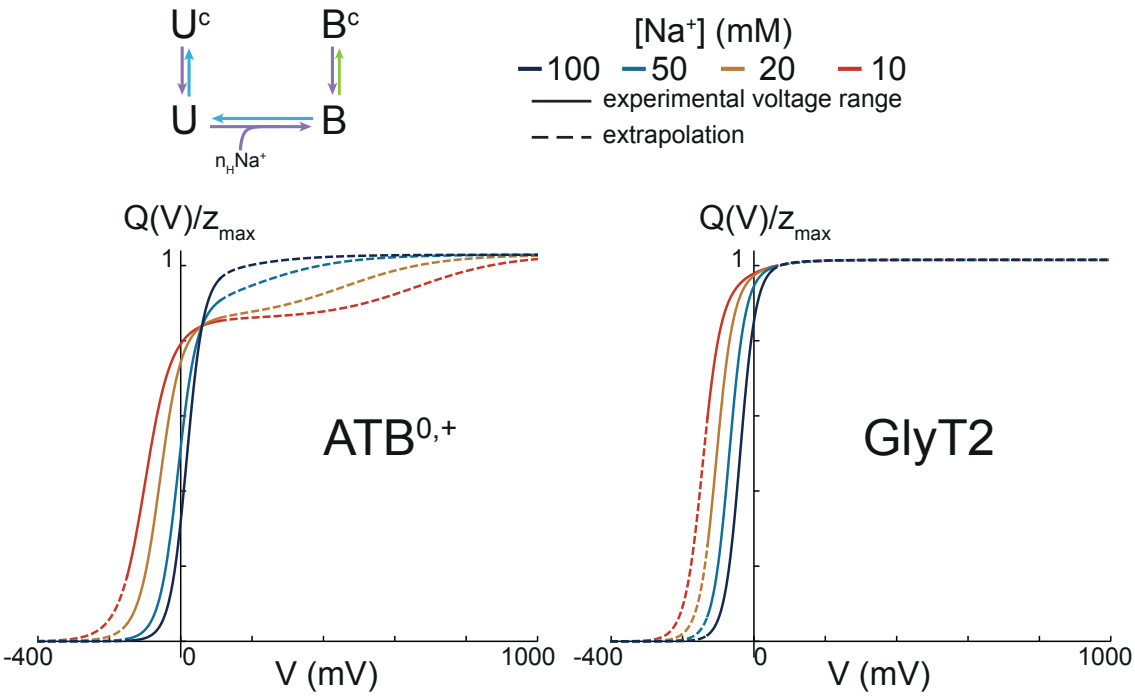

Figure 6–Figure supplement 5. Prediction from the scheme #3 shows a reduction of the apparent Q_{max} at low Na^+ concentration **Figure 6**D . Here, we show the extrapolation of $ATB^{0,+}$- and GlyT2 *Q-V*(s) calculated for an extreme voltage range (−0.4–1 V)using the same set of parameters depicted in **Figure 6**B-C. As expected for the equilibrium equation of scheme #3 , all four *Q-V*s converge to 1 at extreme positive potential.

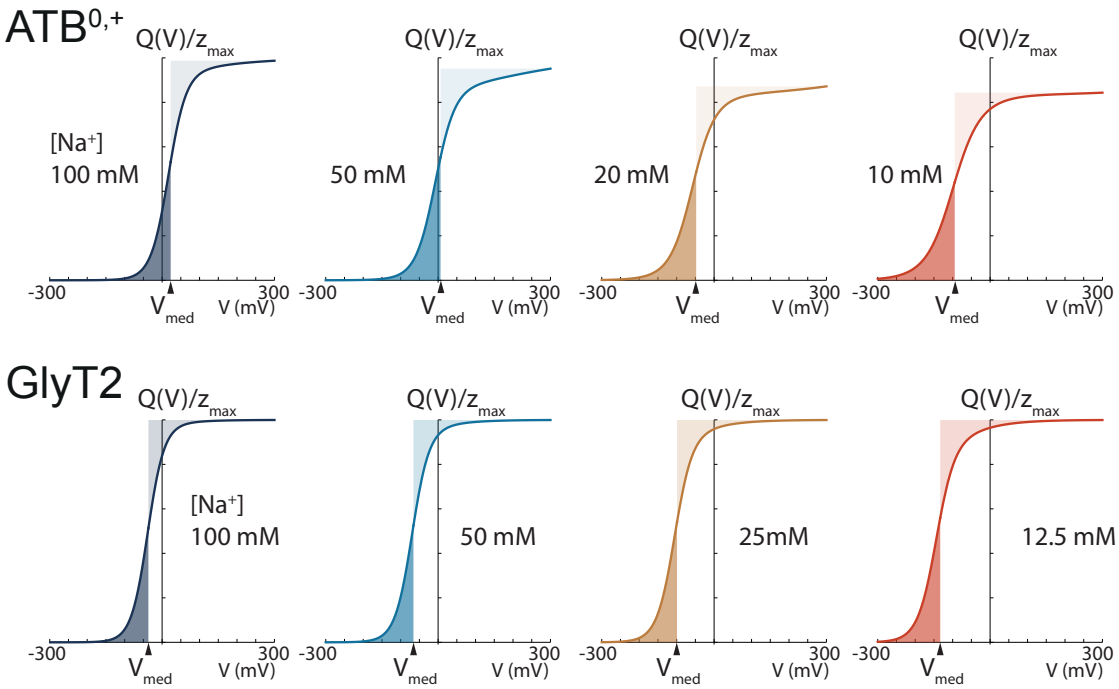

Figure 6–Figure supplement 6. The *Q-V*s of $ATB^{0,+}$ (top) and GlyT2 (bottom) are plotted for four Na^+ concentrations as indicated, using the fit parameters of scheme #3. The median voltage ($V_{med.}$) for equal charge distribution is estimated by numerical integration as described in methods and indicated on the voltage axis of each plot. The darker and lighter shade areas represent the negative and positive integrals, respectively.